This work aims to study numerically annular flows in vertical pipes. Four numerical simulations were performed using the OpenFoam software for the reproduction of three experimental cases presented by WOLF, JAYANTI and HEWITT (2001). To perform the numerical simulations, the multiphaseEulerFoam algorithm was used.

Advisor: Marcus Vinícius Canhoto Alves

Joinville, 2020

YEAR 2020

MARCOS VINÍCIUS SALLES | NUMERICAL SIMULATION OF THE VERTICAL ANNULAR GAS-LIQUID TWO-PHASE FLOW

UDESC
**UNIVERSITY OF SANTA CATARINA STATE - UDESC**
**TECHNOLOGICAL SCIENCE CENTER - CCT**
**MASTER'S DEGREE IN MECHANICAL ENGINEERING**

MASTERS DISSERTATION

# NUMERICAL SIMULATION OF THE VERTICAL ANNULAR GAS-LIQUID TWO-PHASE FLOW

Marcos Vinícius Salles

Joinville, 2020

**MARCOS VINÍCIUS SALLES**

# NUMERICAL SIMULATION OF THE VERTICAL ANNULAR GAS-LIQUID TWO-PHASE FLOW

Dissertação apresentada ao Curso de Mestrado do Programa de Pós-Graduação em Engenharia Mecânica, Área de Concentração em Análise e Simulação Numérica, da Universidade do Estado de Santa Catarina (UDESC), como requisito parcial para obtenção de grau de **Mestre em Engenharia Mecânica**

**Orientador: Marcus Vinícius Canhoto Alves**

Joinville, SC, Brasil

2020

Salles, Marcos Vinícius
NUMERICAL SIMULATION OF THE VERTICAL ANNULAR GAS-LIQUID TWO-PHASE FLOW / Marcos Vinícius Salles. -- 2020.
80 p.

Orientador: Marcus Vinícius Canhoto Alves
Dissertação (mestrado) -- Universidade do Estado de Santa Catarina, Centro de Ciências Tecnológicas, Programa de Pós-Graduação em Engenharia Mecânica, Joinville, 2020.

1. Annular flow. 2. Two-phase flow. 3. OpenFoam. I. Alves, Marcus Vinícius Canhoto. II. Universidade do Estado de Santa Catarina, Centro de Ciências Tecnológicas, Programa de Pós-Graduação em Engenharia Mecânica. III. Título.

**Numerical Simulation of the Vertical Annular Gas-Liquid Two-phase Flow**

por

**Marcos Vinicius Salles**

Esta dissertação foi julgada adequada para obtenção do titulo de

**MESTRE EM ENGENHARIA MECÂNICA**

Área de concentração em "Modelagem e Simulação Numérica"
e aprovada em sua forma final pelo

CURSO DE MESTRADO ACADÊMICO EM ENGENHARIA MECÂNICA
DO CENTRO DE CIÊNCIAS TECNOLÓGICAS DA
UNIVERSIDADE DO ESTADO DE SANTA CATARINA.

Banca Examinadora:

Prof. Dr. Marcus Vinícius Canhoto Alves
CCT/UDESC (Orientador/Presidente)

Profa. Dra. Talita Sauter Possamai
UFSC/Joinville

Prof. Dr. Paulo Sergio Berving Zdanski
CCT/UDESC

**Joinville,SC, 14 de fevereiro de 2020.**

## ACKNOWLEDGMENT

I would like to thank to my whole Family for everything.

I would like to thank to my friends for their support.

I would like to thank to Prof. Marcus Vinícius Canhoto Alves, for his supervision, advice, partnership, patience and for offering me this very interesting study subject. I hope this partnership can endure for the years to come.

To the State University of Santa Catarina – UDESC and the Department of Mechanical Engineering for the opportunity. To the Department of Computer Science for providing a virtual machine to carry out some simulations.

To the Coordination for the Improvement of Higher Education Personal – CAPES for the Master Scholarship at UDESC (grant CAPES 001).

To the Nacional Council of Scientific and Technological Development for funding this work and for the overall support to our laboratory (grant CNPq 43382020187).

To the Santa Catarina Research Foundation – FAPESC for funding this work and for the overall support to our laboratory (grants: FAPESC 2019TR000779 and FAPESC 2019TR000783). FAPESC is also responsible for the support and funding of the LabP2D – "Laboratório de Processamento Paralelo Distribuído do CCT/UDESC".

The members of LabP2D are also acknowledged by the support and advice.

This work used the computational resources of the "Centro Nacional de Processamento de Alto Desempenho em São Paulo (CENAPAD-SP)". An acknowledgment I also due to the support technicians from CENAPAD-SP that worked along us for several days to help in trying to make our applications work correctly.

The São Paulo Research Foundation – FAPESP is also acknowledged as it supports CENAPAD-SP and funded the installations for the Centre.

**RESUMO**

Dissertação de Mestrado
Programa de Pós-Graduação em Engenharia Mecânica
Universidade do Estado de Santa Catarina

**NUMERICAL SIMULATION OF THE VERTICAL ANNULAR GAS-LIQUID TWO-PHASE FLOW**

AUTHOR: MARCOS VINÍCIUS SALLES
ORIENTADOR: MARCUS VINÍCIUS CANHOTO ALVES
Joinville, 14 de fevereiro de 2020

Escoamentos anulares em dutos verticais estão presentes em diversas aplicações industriais como, por exemplo, em trocadores de calor, reatores nucleares e na extração de petróleo e gás natural. Este trabalho tem como objetivo estudar numericamente escoamentos anulares em dutos verticais. Foram realizadas quatro simulações numéricas utilizando o software OpenFoam para a reprodução de três casos experimentais apresentados no trabalho de WOLF, JAYANTI e HEWITT (2001). Estes autores realizaram experimentos de escoamentos anulares em um duto vertical de 10,78 [m] de comprimento e com 31,8 [mm] de diâmetro interno, utilizando ar-água com diferentes fluxos de massa para ambos os fluidos. Para a realização das simulações numéricas foi utilizado o algoritmo multiphaseEulerFoam, o qual foi desenvolvido através do acoplamento entre o modelo de dois fluidos e o método dos volumes de fluidos (VOF) e utiliza o método de compressão de interface para capturar a mesma. As simulações numéricas apresentaram bons resultados para a parte inicial do duto. Contudo, a partir de uma certa posição, deficiências na captura da interface entre as duas fases começaram a surgir e, devido a isto, o filme líquido começou a pulverizar, acarretando, assim, em uma não convergência entre os resultados numéricos e experimentais nestas regiões.

**Palavras-chave**: Escoamento anular, OpenFoam, multiphaseEulerFoam, Escoamento bifásico

**ABSTRACT**
Master's Dissertation
Programa de Pós-Graduação em Engenharia Mecânica
Universidade do Estado de Santa Catarina

**NUMERICAL SIMULATION OF THE VERTICAL ANNULAR GAS-LIQUID TWO-PHASE FLOW**
AUTHOR: MARCOS VINÍCIUS SALLES
ADVISER: MARCUS VINÍCIUS CANHOTO ALVES
Joinville, xx February 2020

Annular flows in vertical pipes are present in several industrial applications such as heat exchangers, nuclear reactors and in the oil and natural gas extraction. This work aims to study numerically annular flows in vertical pipes. Four numerical simulations were performed using the OpenFoam software for the reproduction of three experimental cases presented by WOLF, JAYANTI and HEWITT (2001). These authors performed annular flow experiments in a vertical pipe with 10.78 [m] long and 31.8 [mm] in internal diameter using air-water with different mass fluxes for both fluids. To perform the numerical simulations, the multiphaseEulerFoam algorithm was used, which was developed through the coupling between the two-fluid model and the volume of fluid method (VOF) and uses the interface compression method to capture the interface between the two phases. The numerical simulations showed good results for the initial part of the pipe. However, from a certain position of the pipe, deficiencies in the interface capture between the two phases began to appear and due to this the liquid film started to pulverize, thus causing a non-convergence between the numerical and experimental results in these regions.

**Keywords**: Annular flow, OpenFoam, multiphaseEulerFoam, Two-phase flow

## LIST OF FIGURES

## LIST OF TABLES

# LIST OF SYMBOLS

| | | |
|---|---|---|
| $A$ | Cross Section Area | $[m^2]$ |
| $C_D$ | Drag Coefficient | |
| $C_O$ | Courant Number | |
| $C_\alpha$ | Interface Compression Coefficient | |
| $CD_{k\omega}$ | Cross diffusion | $\left[\frac{Pa}{m^2}\right]$ |
| $d_d$ | Droplet Diameter | $[m]$ |
| $D_H$ | Hydraulic Cross Section Diameter | $[m]$ |
| $F_1$, $F_2$ | Coupling Functions | |
| $\vec{F}_D$ | Drag Force | $[N]$ |
| $\vec{F}_s$ | Surface Tension Force | $[N]$ |
| $\vec{g}$ | Gravity Acceleration | $\left[\frac{m}{s^2}\right]$ |
| $I$ | Turbulent Intensity | $[\%]$ |
| $k$ | Turbulent Kinetic Energy | $\left[\frac{m^2}{s^2}\right]$ |
| $\ell$ | Turbulent Scale Length | $[m]$ |
| $m$ | Mass | $[kg]$ |
| $M$ | Molar mass | $\left[\frac{g}{mol}\right]$ |
| $\dot{M}$ | Mass Flow | $\left[\frac{kg}{s}\right]$ |
| $n$ | Number of Moles | $[mols]$ |
| P | Pressure | $[Pa]$ |
| $\tilde{P}$ | Turbulent Kinetic Energy Production | $\left[\frac{Pa}{s}\right]$ |
| $\vec{Q}$ | Volumetric Flow | $\left[\frac{m^3}{s}\right]$ |
| $R$ | Ideal Gas Constant | $\left[\frac{J}{K.mol}\right]$ |
| $Re$ | Reynolds Number | |
| $s$ | Slip Ratio | |

| | | |
|---|---|---|
| $S$ | Invariant Measure of Strain Rate | $\left[\frac{1}{s}\right]$ |
| $t$ | Time | $[s]$ |
| $T$ | Temperature | $[K]$ |
| $\vec{U}$ | Phase Velocity | $\left[\frac{m}{s}\right]$ |
| $\vec{U}_c$ | Compression Velocity | $\left[\frac{m}{s}\right]$ |
| $\vec{U}_{ref}$ | Reference Velocity | $\left[\frac{m}{s}\right]$ |
| $\vec{U}_s$ | Superficial Velocity | $\left[\frac{m}{s}\right]$ |
| $\vec{U}_{sl}$ | Slip Velocity | $\left[\frac{m}{s}\right]$ |
| $V$ | Volume | $[m^3]$ |
| $y$ | Distance to Nearest Wall | $[m]$ |

## GREEK SYMBOLS

| | | |
|---|---|---|
| $\alpha$ | Volume Fraction | |
| $\kappa$ | Surface Curvature | $[m]$ |
| $\mu$ | Dynamic Viscosity | $[Pa.s]$ |
| $\nu$ | Kinematic Viscosity | $\left[\frac{m^2}{s}\right]$ |
| $\rho$ | Specific Mass | $\left[\frac{kg}{m^3}\right]$ |
| $\bar{\rho}$ | Apparent Density | $\left[\frac{kg}{m^3}\right]$ |
| $\sigma$ | Surface Tension Coefficient | $\left[\frac{N}{m}\right]$ |
| $\omega$ | Specific turbulent Dissipation Rate | $\left[\frac{1}{s}\right]$ |

## SUBSCRIPTS

| | |
|---|---|
| $c$ | Continuous Phase |
| $d$ | Dispersed Phase |

| | |
|---|---|
| $G$ | Gas |
| $k$ | One of the Flow Phases (Liquid or Gas) |
| $L$ | Liquid |
| $m$ | Mixture |
| $t$ | Turbulent |

**CONTENTS**

# 1 INTRODUCTION

Vertical gas-liquid flow in pipes and tubes are present in several industrial applications such as heat exchangers, nuclear reactors and in the oil and natural gas extraction. There are several studies in the literature regarding this type of flow, however, most of them present empirical correlations or simplified models for the calculation of the flow properties either in the steady state or transient conditions. More recent studies have applied modern computational tools that allowed to simulate and evaluate these flows more accurately and precisely considering tridimensional effects, influence of turbulence and transient flow conditions.

The flow of gas-liquid mixtures (and two-phase flows in general) are highly influenced by the interfacial topology that separates the phases. This interfacial topological arrangement is by nature a transient phenomenon, however, it can be treated statistically in a similar way as turbulence. Due to the complex nature of the interfacial behavior the observation of the phenomenon was crucial for its understanding. Through experimental visualization studies performed in the 1960`s it was stablished that some topological patterns were mostly dominant, and had very distinct characteristics and behavior (WALLIS, 1969). For gas-liquid flows WALLIS (1969) suggested the use of 4 distinct so-called flow patterns: bubble flow; slug flow; churn flow and annular flow.

Of the flow patterns presented the most relevant (BARBOSA, 2001; WALTRICH, 2013; ALVES, 2014) is the annular flow. The study of annular flows is particularly important due to the fact that heat exchangers often make use of phase-change to increase the convection heat transfer coefficient improving the overall heat transfer efficiency, reducing size and material cost. A more detailed description of the flow patterns, in particular the annular flow pattern, is presented later in the text.

## 1.1 Objectives

The main goal of the present work is to simulate numerically some of the cases presented in the experimental work of WOLF, JAYANTI and HEWITT (2001). This experimental work is taken as a basis for this work because it presents 28 air-water annular flow experiments with different mass flows rates in a vertical pipe with 10.78 [m] long and 31.8 [mm] in internal diameter test section. The test section is instrumented with several sensors for static pressure, core void fraction (liquid film thickness) and inlet mass flow rates.

The numerical simulations use the hybrid algorithm for an Eulerian-Eulerian-VOF model called multiphaseEulerFoam which is implemented in the OpenFoam software. The OpenFoam software is a free open source computer program developed in C++. This algorithm was developed through the coupling between the tridimensional two-fluid model and the volume of fluid method (for tracking of a sharp interface) and uses an interface compression method to capture the interface. The simulations were carried out using air-water in a transient, turbulent, isothermal regime and with constant thermophysical properties throughout the entire pipe.

The present work is the beginning of a larger study being carried out at the Department of Mechanical Engineering of the Santa Catarina State University (UDESC) in southern region of Brazil. This is the first stage of the project and focused in the evaluation of the methodology applied in the simulation of annular flows in vertical pipes. This work will form the basis for the next stages of the project, that include the simulation of other experimental results obtained in different facilities that are available throughout the open literature.

## 1.2 Structure of the text

This work is organized as 5 chapters, including this Chapter 1 (Introduction). The subsequent chapters are organized as follows:

- Chapter 2 presents a review of the literature on annular flows with theoretical, experimental and numerical works.

- Chapter 3 describes the mathematical modeling employed in the multiphaseEulerFoam algorithm to carry out the numerical simulations.
- Chapter 4 presents the boundary conditions, the mesh and some parameters that are necessary to perform the simulations.
- Chapter 5 presents the results and some analyzes obtained through the numerical simulations.
- Chapter 6 presents the conclusions and recommendations for future works.

# 2 LITERATURE REVIEW

This section presents some basic concepts of two-phase flows, the main gas-liquid flow patterns in vertical pipes, a detailed description of the annular flow pattern and some of the various studies presented in the literature about annular flows that were used as theoretical basis for the elaboration of this work.

## 2.1 Multiphase Flows

The phase of a substance generally refers to its state of matter, in other words, whether the material is in the solid, liquid or gaseous phase. Multiphase flows are flows that have a mixture of two or more substances in different phases, such as gas bubbles or solid particles in a continuous liquid phase; liquid droplets or solid particles in a continuous gas phase, and so on. It does however, extend this simple definition due to the particular interfacial interaction between two substances in the liquid form. Gases, liquids and solids are, in essence different phases, but two liquids may not mix with each other and behave as being two different phases. A more objective definition of phase must elaborate on this physical state concept. An elegant way is to consider a phase any portion of matter with homogeneous thermophysical properties that is separated from other substances with different thermophysical properties by an interface.

Multiphase gas-liquid flows can be generically classified into two categories: dispersed flows and segregated flows. Dispersed flows are flows in which one of the phases consists of discrete particles, such as gas bubbles, liquid droplets or solid particles. Segregated flows are flows where the two phases are separated by a continuous interfacial surface, that is, it is possible to move from one point to another distant point in space in the same phase while remaining in the same medium. The definitions presented in the subsection 2.1 were based on the ones presented and discussed in CROWE (2006).

### 2.1.1 VOLUME FRACTION AND SPECIFIC MASS

The volume fraction of each phase of the mixture is defined as the ratio between the pipe cross-sectional area occupied by phase *k* and the total pipe cross-sectional area, this can be mathematically expressed according to Equation 1.

$$\alpha_k = \lim_{\delta V \to V^0} \frac{\delta V_k}{\delta V} \tag{1}$$

The subscript *k* refers to the fluid phase. The terms $V_k$, $V$, $A_k$ e $A$ are the phase *k* volume, the mixture volume, the pipe cross-sectional area occupied by phase *k* and the total pipe cross-sectional area, respectively. By definition the sum of the liquid and gas volume fractions should be unitary.

$$\alpha_L + \alpha_G = 1 \tag{2}$$

The apparent or the mixture specific mass of phase *k* is defined by the ratio of the mass of this phase per unit volume of the mixture. This property can also be related through the fluid specific mass and the volume fraction as,

$$\overline{\rho_k} = \lim_{\delta V \to V^0} \frac{\delta m_k}{\delta V} = \alpha_k \rho_k \tag{3}$$

Where $m_k$ e $\rho_k$ are the mass and specific mass of phase *k*, respectively. The mixture specific mass is defined as the sum between the apparent specific masses of the two phases.

$$\rho_m = \alpha_L \rho_L + \alpha_G \rho_G \tag{4}$$

The subscripts *L*, *G* and *m* refer to the liquid and gas phases and the mixture, respectively.

### 2.1.2 PHASE AND SUPERFICIAL VELOCITIES

In two-phase flows the phase superficial velocity is defined as the velocity of the phase *k* if it was the only phase flowing within the pipe. In mathematical terms its definition is given by the ratio between the mass flow rate of the phase *k* by the product of the pipe cross-sectional area and the specific mass of the fluid, as described in Equation 5.

$$\vec{U}_{s,k} = \frac{\dot{M}_k}{\rho_k A} = \frac{\vec{Q}_k}{A} \tag{5}$$

Where $\dot{M}_k$ e $Q_k$ are the mass flow rate and the volumetric flow rate of phase *k*, respectively.

The phase velocity is similar to the superficial velocity, but just considers the cross-sectional area occupied by the phase *k*.

$$\vec{U}_k = \frac{\dot{M}_k}{\rho_k A_k} = \frac{\vec{Q}_k}{A_k} \tag{6}$$

The superficial and phase velocities are related through the phase fraction, according to Equation 7.

$$\vec{U}_{s,k} = \alpha_k \vec{U}_k \tag{7}$$

The mixture velocity is defined as the sum of the superficial velocities of the two phases.

$$\vec{U}_m = \vec{U}_{s,G} + \vec{U}_{s,L} \tag{8}$$

The difference and the ratio between the phase velocities present in the flow are defined as the slip velocity and the slip ratio, respectively, and are defined according to Equations 9 and 10.

$$\vec{U}_{sl} = \left|\vec{U}_G - \vec{U}_L\right| \quad (9)$$

$$s = \frac{\vec{U}_G}{\vec{U}_L} \quad (10)$$

## 2.2 Two-Phase Gas-Liquid Flow Patterns

Two-phase gas-liquid flows in vertical pipes may have different flow patterns. These patterns are related with some parameters such as pipe diameter and orientation, fluid properties, gas and liquid flow rates, among others. The main gas-liquid flow patterns in vertical pipes are bubble flow, slug flow, churn flow and annular flow, which are illustrated in Figure 1.

The bubble flow is characterized by a continuous liquid phase and a gas phase dispersed within the liquid in the form of bubbles. The gas bubbles are nonuniform in size and move with complex movement within the fluid. As the gas flow rate increases the number of bubbles, the diversity in shape and the difference in bubble velocities increase, inducing to more frequent collisions between bubbles, thus leading to bubble coalescence (ABDULKADIR, 2011). This process will eventually lead to the formation of a Taylor bubble, this marks the transition from bubble to slug flows (WALLIS, 1969).

The slug flow is characterized by the presence of Taylor bubbles which are large bullet shaped bubbles that occupy almost the entire cross section of the pipe. The Taylor bubbles flow upwards and are surrounded by a falling liquid film. These bubbles are separated from each other by an upwardly flowing liquid region that is defined as liquid slug. This liquid slug may contain dispersed gas bubbles (ABDULKADIR, 2011). These bubbles in the liquid slug are highly distorted and are trapped behind the Taylor bubble by a vortex created from the discharge of the film in the slug. These vortexes are intense and can ripe the interface between gas and liquid at the end of the Taylor bubble, forming the small distorted bubbles in the slug (WALLIS, 1969; CACHARD and DELHAYE, 1996).

The churn flow has an oscillatory nature and is a highly disordered and chaotic. Starting from a stable slug flow, and increasing gas flow rates, the Taylor bubbles become unstable and break up, giving rise to a continuous gas core with lots of droplets and filaments of liquid

present in the gas flow. An oscillating liquid film is formed at the wall, with alternating liquid mas flow direction. At a fixed section of the pipe, at times the liquid film descends, accumulating in a region upstream of the point being observed. At some point this accumulation reaches a critical point in which a high amplitude waves travels downstream, producing an ascending net flow of liquid transport.

Figure 1 - Representation of the main two-phase gas-liquid flow patterns in vertical pipes.

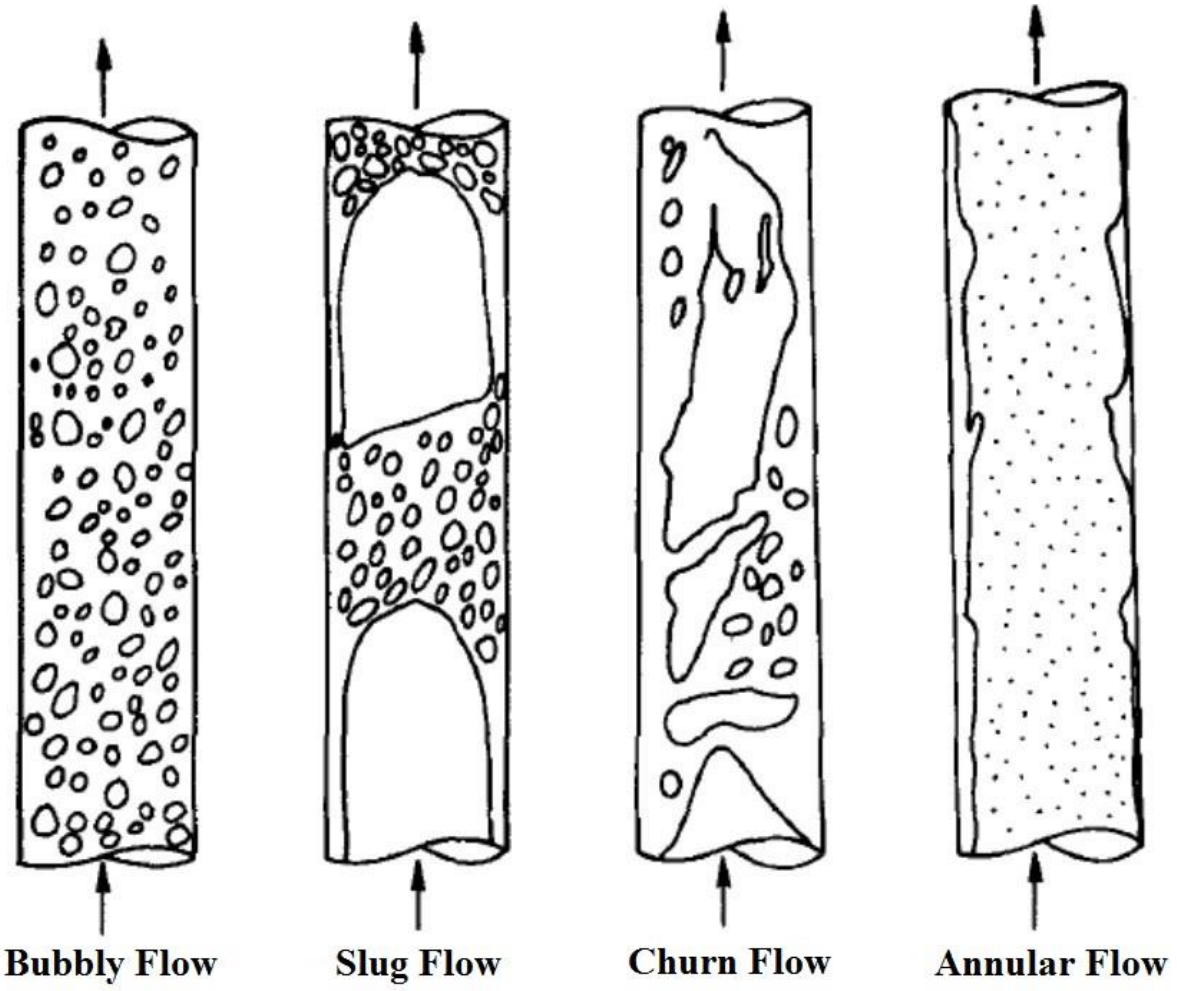


Source: TAITEL, BARNEA and DUKLER (1980).

As the gas flow rate increases the interfacial shear forces between gas and liquid increases, leading to a more stable condition, with less liquid flowing in the form of droplets and a stable ascending liquid film at the pipe walls, characterizing an annular flow condition.

The annular flow consists of a gas core, which flows at high velocities in the central region of the pipe, and a liquid film adjacent to the pipe walls, which surrounds the gas core and flows at lower velocities. Ripples appear at the gas-liquid interface (or core-film interface) due to the presence of interfacial shear forces. Liquid droplets are drawn from the wave crest and become entrained in the gas core, accelerating to almost the same velocity of the gas (ALVES, 2014). These droplets are subsequently deposited back into the liquid film downstream of the entrainment point, producing a liquid transport inside the gas core. The shear forces present in the phase interface become dominant over the gravitational forces, so the gas core can drag all the liquid upwards without any oscillation (ABDULKADIR, 2011; ALVES, 2014).

## 2.3 Annular Flow

In this subsection some theoretical, experimental and numerical studies about annular flows are presented. The first subtopic was divided into experimental and mathematical modeling works. This organization was used because many of the mathematical models for the calculation of annular flow properties rely on closure relations that are derived from experimental data. The second subtopic presents numerical studies, which present the development of algorithms and numerical simulations to solve annular flows.

### 2.3.1 EXPERIMENTAL AND MATHEMATICAL MODELING WORKS

BERTODANO, JAN and BEUS (1997) performed annular air-water flow experiments in a vertical pipe test section with 9.5 [mm] in internal diameter and 4.2 [m] long. Figure 2 schematically illustrates the test facility used in these experiments. The authors considered in their experiments a pressure range between 140 - 660 [kPa] and air and liquid mass flow rates between 0.0028 - 0.028 [kg/s] and 0.0053 - 0.038 [kg/s], respectively. The goal of this work was to provide new data regarding annular flows under new flow conditions, using higher pressures and gas velocities than most experiments performed until then.

WOLF, JAYANTI, and HEWITT (2001) conducted experimental studies of annular air-water flows in a vertical pipe test section with 10.78 [m] long and 31.8 [mm] in internal diameter. Figure 3 schematically illustrates the test facility used in these experiments. The authors presented, graphically and tabularly, the values of several flow parameters for different gas and liquid mass flow rates at the pipe inlet. The results showed that the liquid film flow rate developed completely within a distance corresponding to 50 pipe diameters and the entrained fraction and the thickness of the liquid film took about 100 to 300 pipe diameters. It was also found that the pressure gradient, the wall shear stress, the liquid film flow rate and the liquid film thickness decreased with the distance traveled by the fluids. This was due to the presence of gravitational forces and the emergence of interfacial waves between the two phases.

WALTRICH, FALCONE and BARBOSA (2013) performed two-phase air-water flow experiments in a vertical pipe test section with 42 [m] long and 48 [mm] in internal diameter. Figure 4 schematically illustrates the test facility used in these experiments. They considered a pressure range between 1.4 - 5.2 [bars], liquid mass flow rate between 17 - 319 [kg.m²/s] and dimensionless gas velocities between 0.05 - 1.6. The data collected in these experiments were used to analyze the axial development of slug, churn and annular flow patterns using correlations present in the literature; the behavior of the volume fraction and the flow structure frequencies. The study also evaluated some empirical relationships present in the literature such as the formulations developed by WALLIS (1969) and TURNER (1969), among others, and proved that these formulations present coherent results when compared to experimental data.

WALTRICH, FALCONE and BARBOSA (2015) conducted experimental studies to investigate the liquid distribution and transport in two-phase gas-liquid flows in a vertical pipe with 42 [m] long and 48 [mm] in internal diameter. Figure 4 schematically illustrates the test facility used in these experiments. The authors also developed a mathematical modeling to estimate the liquid hold-up in vertical wells through a pseudo-permanent approximation. The results obtained from this mathematical model were compared with the experimental data and presented a variation of up to ± 25%.

ALIYU et al. (2017) conducted experimental studies of annular air-water flows in a vertical pipe teste section with 20 [m] long and 101.6 [mm] in internal diameter. Figure 5

schematically illustrates the test facility used in these experiments. The gas and liquid superficial velocities ranges evaluated in these experiments were 11 - 29 [m/s] and 0.1 - 1 [m/s], respectively. In addition to the data obtained in these experiments, the authors also collected data from similar experiments with different flow conditions present in the literature for the development of a mathematical model to estimate the interfacial friction factor in annular flows in small and large diameter pipes. This new formulation was able to estimate the interfacial friction factor with a maximum absolute mean error of 28.1%.

Figure 2 - Test facility used in the experiments of BERTODANO, JAN and BEUS (1997).

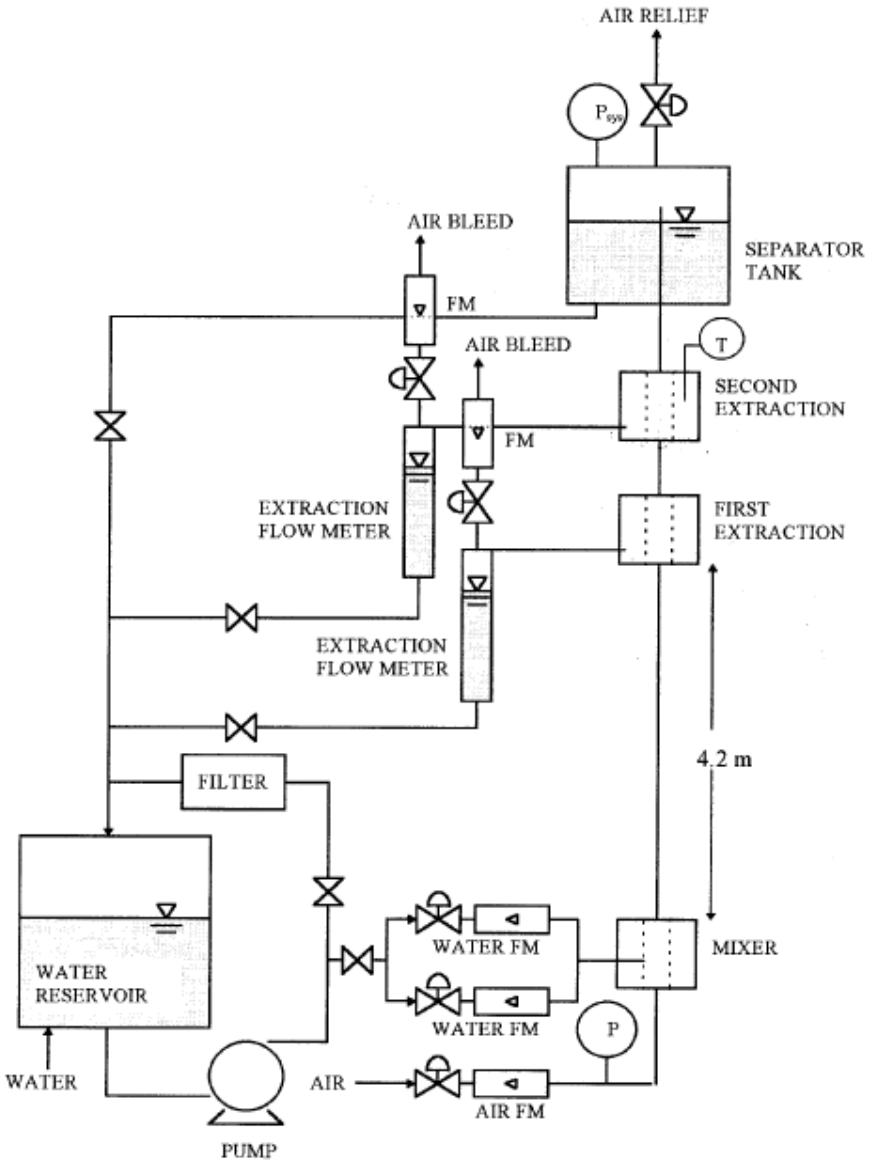


Source: BERTODANO, JAN and BEUS (1997).

Figure 3 - Test facility used in the experiments of WOLF, JAYANTI, and HEWITT (2001).

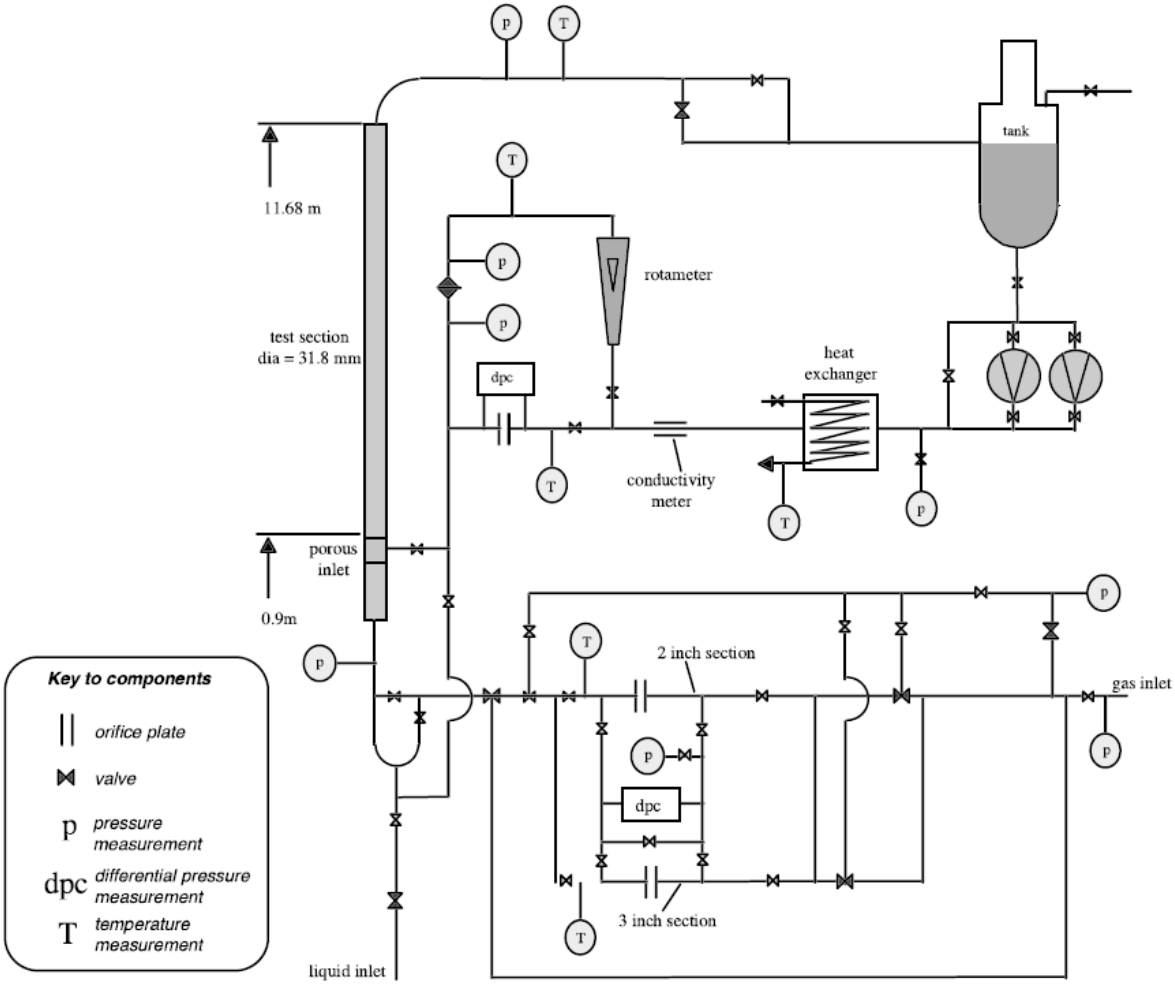


Source: WOLF, JAYANTI and HEWITT (2001).

CHEN et al. (2017) studied churn and annular flow patterns features through experiments conducted in a vertical pipe teste section using air-water at atmospheric pressure and with superficial air and water velocities ranging from 5.1 - 30 [m/s] and 0.04 - 0.4 [m/s], respectively. Figure 6 schematically illustrates the test facility used in these experiments. The authors developed a simple model using the pressure differential and void fraction transients to identify the transition boundaries between churn and annular flow patterns. Simple statistical operations were used to analyze these data. The flow regimes were identified through specific trends and behaviors present in the curves obtained in the statistical analyzes. The results obtained by this new technique are in agreement with flow regime maps present in the literature.

POSADA and WALTRICH (2018) experimentally studied the effects of induced low frequency oscillations on two-phase air-water flows in a vertical pipe with 42 [m] long and 48 [mm] in internal diameter. Figure 4 schematically illustrates the test facility used in these experiments. The authors considered the churn, annular flow patterns and the transition between them with liquid and gas superficial velocities ranging from 0.017 - 0.3 [m/s] and 4 - 21 [m/s], respectively. Flow regimes observations under oscillatory effects showed significant differences when compared to steady state flows under similar conditions. For oscillatory flows with a pressure of 210 [kPa], the churn flow regime was observed, while for similar steady state conditions the annular flow was observed. Other cases similar to this also occurred for lower pressures. It has been found that the pressure gradient in the oscillatory flows may be significantly lower than in steady state for low superficial gas and liquid velocities, which is a consequence of the formation of large liquid waves at the inlet due to induced oscillations in the gas injection.

AL-SARKHI, SARICA and QURESHI (2012) developed a methodology to estimate the entrainment fraction in annular gas-liquid flows in vertical, horizontal and inclined pipes. The authors performed a bibliographic study of similar works present in the literature. They found that other formulations with the same purpose elaborated by other authors had a deficiency in estimating the maximum entrainment rate at low liquid Reynolds numbers. The methodology developed in this study sought to correct the problem mentioned previously and the results obtained through this method were consistent when compared with experimental data present in the literature.

PAGAN and WALTRICH (2016) developed a simplified model to predict the liquid hold-up at the bottom of gas production wells. This model was based on the modification of the pipeline performance relation by applying the nodal analysis technique. This new correlation is simple and allows to accurately predict the initiation of the liquid hold-up at the bottom of the wells and the time in which production will cease after the onset of this phenomenon. Field data using pipelines with internal diameters ranging from 72.9 - 154.7 [mm] and with pressures ranging from 6 - 98 [bars] were used for comparative purposes and an average absolute error of 17% was found.

PAGAN et al. (2017) developed a mathematical model to estimate the interfacial friction factor in two-phase gas-liquid flows in vertical and near vertical pipes with small and

large diameters for churn and annular flow patterns. This model was obtained through modifications of similar empirical correlations proposed by other authors for pipes with small diameters. This new formulation showed good results under different flow conditions, which covered pipes with diameters ranging from 31.8 - 279 [mm], pressures ranging from 1 - 613 [bars] and combinations of air-water and oil-natural gas fluids. The absolute mean error in estimating the pressure gradient decreased from 155% to 36% after the modifications of the original models.

Figure 4 - Test facility used in the experiments of WALTRICH, FALCONE and BARBOSA (2013).

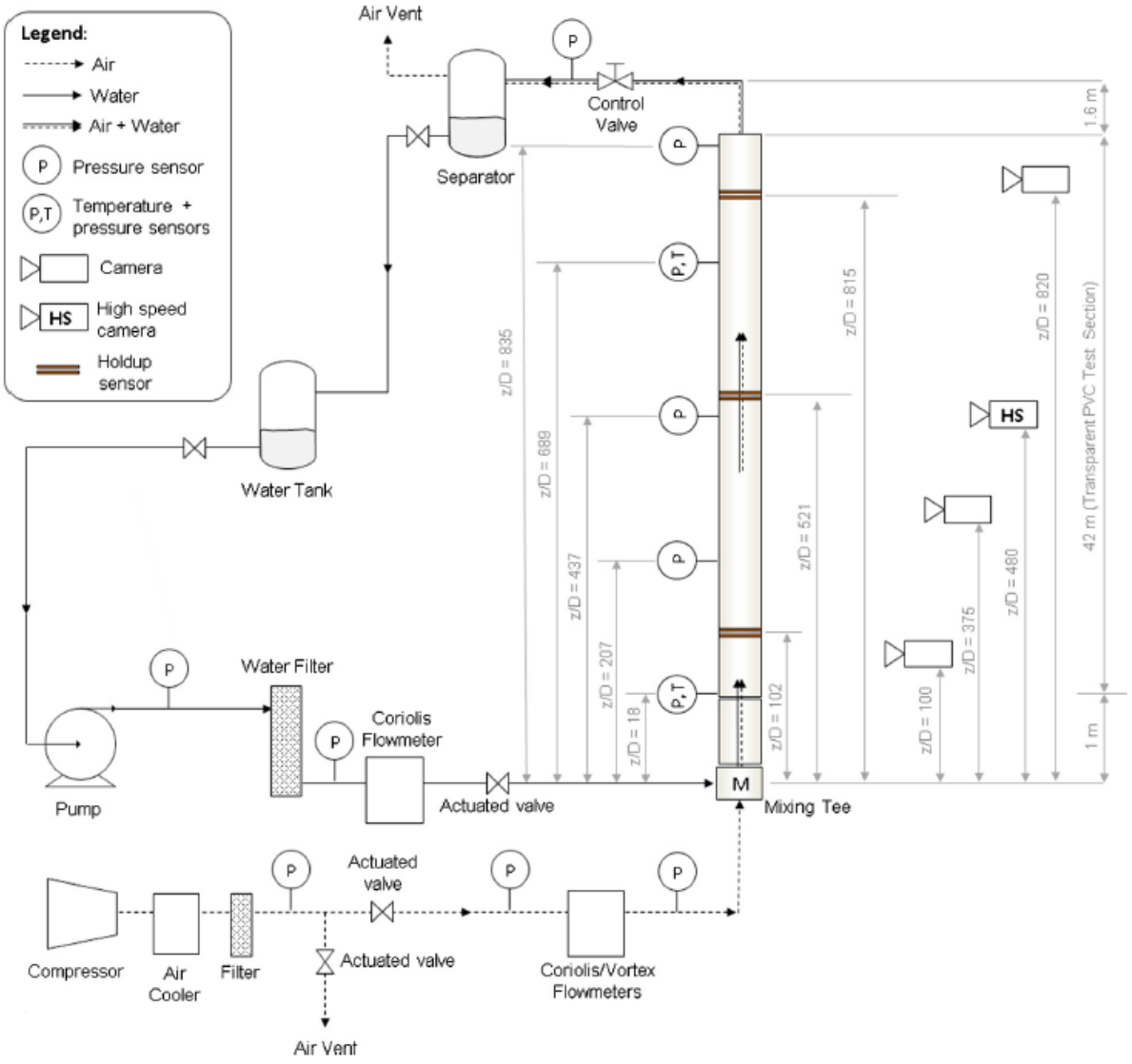


Source: WALTRICH, FALCONE and BARBOSA (2013).

Figure 5 - Test facility used in the experiments of ALIYU et al. (2017).

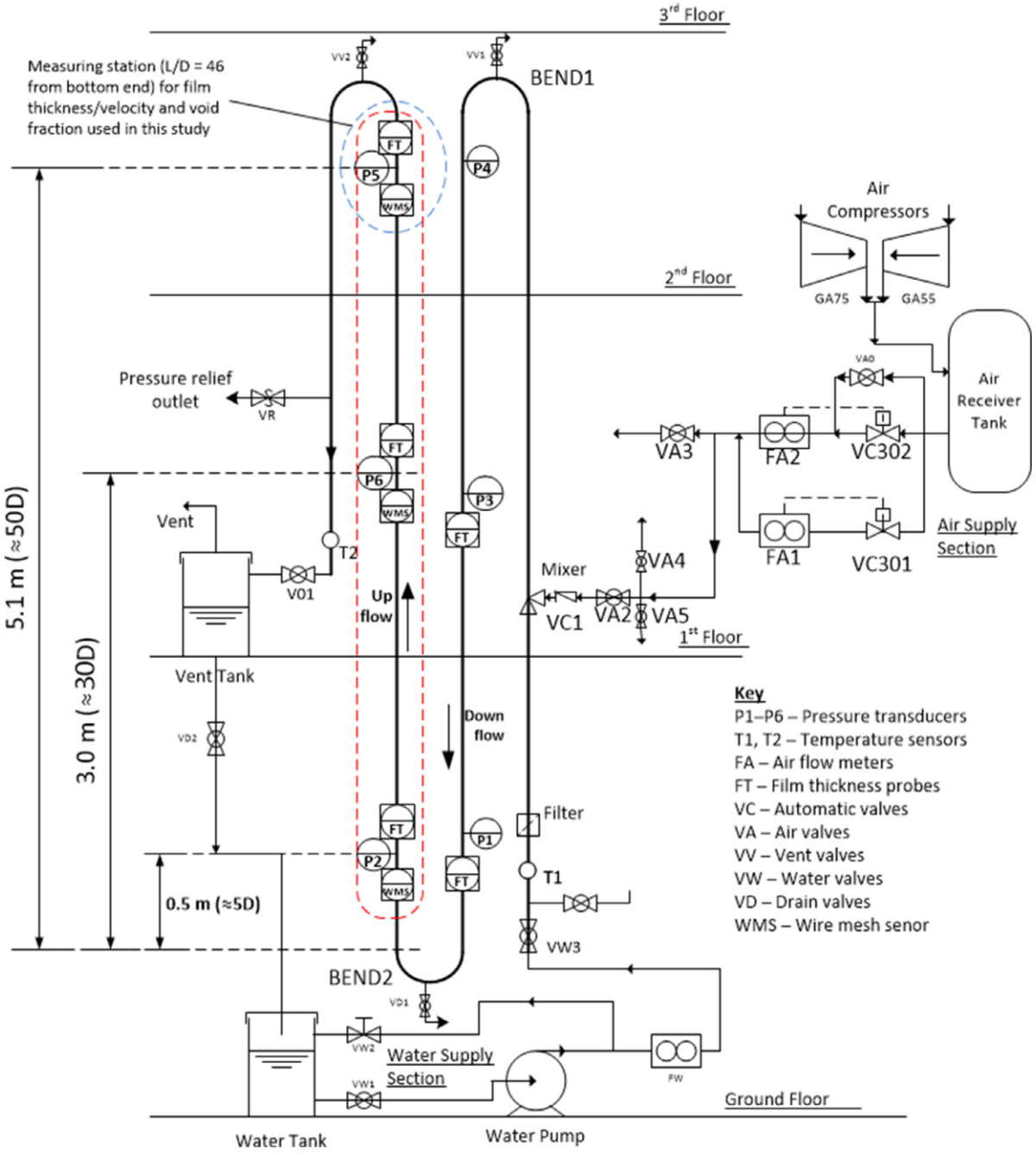


Source: ALIYU et al. (2017).

LIU and BAI (2017) developed a mathematical model to estimate the droplet entrainment rate in annular flows considering the perturbation wave features. The authors analyzed the influence of the main parameters that characterize these waves on the entrainment rate. It was found that the liquid and gas flow rate, hydraulic diameter, surface tension and the

pressure exert great influence on the wave properties such as critical wavelength, wave amplitude and wave velocity and therefore also had a strong influence on the droplet entrainment rate. For the development of the mathematical model presented in this work, a database was collected in the literature containing pipes with internal diameter up to 42 [mm], air-water flows at low pressures and steam-water flows with pressures up to 9 [ MPa]. The results obtained from this new model showed a maximum deviation of approximately 25% when compared to experimental data.

Figure 6 - Test facility used in the experiments of CHEN et al. (2017).

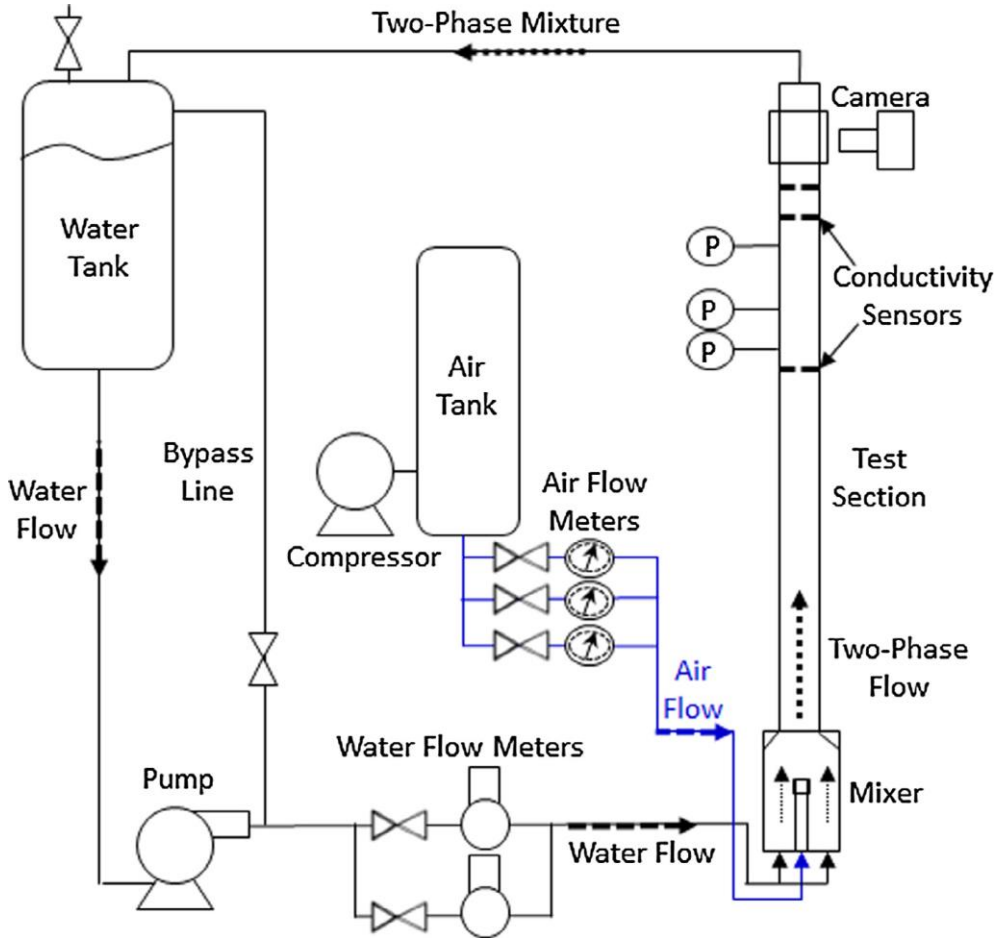


Source: CHEN et al. (2017).

VAN NIMWEGEN, PORTELA and HENKES (2018) developed a mathematical model to estimate the pressure gradient in annular air-water flows in vertical pipes with the addition of surfactants in the flow. The main effect of the presence of surfactant in the flow is

the formation of a foam layer between the gas core and the liquid film. In order to solve the governing equations for this type of problem, four closure relationships were developed which deal with the specific foam mass, the foam viscosity, the gas and film interfacial friction and the liquid layer thickness adjacent to the wall. The results obtained from this new model were compared with experimental data. For 50 and 80 [mm] diameter pipes, the model presented satisfactory results with errors less than 25%. However, due to certain simplifications used for the development of this formulation, errors up to 25% were found for the 34 [mm] diameter pipe.

### 2.3.2 NUMERICAL WORKS

CERNE, PETELIN and TISELJ (2001) developed a hybrid numerical method to solve two-phase flows, which coupled the volume of fluid (VOF) and the two-fluid methods. The volume of fluid method was used in the computational domain regions where the mesh was capable to capture the interface. In regions where the flow had a very dispersed behavior, the two-fluid method was applied. The LVIRA algorithm was used to reconstruct the interface. The coupling between these models was performed through the volume fraction of one of the fluids, which is a common parameter between these two methods. For testing purposes, this algorithm was used to solve the Rayleigh-Taylor instability and an idealized vortex flow. The numerical results obtained by this new method were more realistic when compared to the volume of fluid method results.

LANE et al. (2010) developed and evaluated a set of self-consistent models for annular flow simulations based on three field analysis. This methodology uses an interfacial shear model that considers the presence of interfacial waves, idealizes the interface structure such that it is consistent with the interfacial shear model and experimental observations, includes three entrainment rate models and provides a functional relationship between theoretical and experimental entrainment rates. This methodology was implemented in a home version of the COBRA-TF code. The results obtained with this algorithm presented a reduction in the relative mean error of the entrainment fraction from 20.2% to 4.5% and the axial pressure gradient from 108.2% to 7.6% when compared with the COBRA-TF original code.

LIU, LI and QUAN (2011) proposed a new two-fluid model to solve annular flows in vertical pipes. The mass and momentum conservation equations were solved in the Fluent 6.3.26 commercial software. The liquid droplet flow and interfacial effects were programmed by the authors within this same software. In this new model the impact of liquid droplets on the flow was taken into account at the interface region between the two phases through the source terms present in the momentum, turbulent kinetic energy and the specific turbulent dissipation rate equations. The droplet effect on the gas core flow was neglected, due to the hypothesis of homogeneous mixture in the core adopted in the model development. This method was tested and compared with experimental data and showed good results.

THAKER and BANERJEE (2013) performed a numerical study to evaluate the development of different two-phase air-water flow patterns in a horizontal pipe with 610 [mm] in diameter and 1.5 [m] long for different gas and liquid velocities. Three-dimensional simulations using the volume of fluid method were performed using the OpenFoam software, which used the interFoam algorithm. The authors observed that in this type of flow the position of the gas-liquid interface varies in relation to time and space and, consequently, this influenced the flow field. The numerical results were compared with experimental data and good agreement between them was obtained.

GUPTA, TURANGAN and MANICA (2016) performed a numerical study on annular oil-water flows in a vertical pipe with 14.2 [mm] in radius and with surface oil velocities ranging from 0.21 - 0.61 [m/s] and with constant water velocity of 0,058 [m/s]. In the simulations were considered the laminar flow regime; a two-dimensional domain, symmetrical with respect to the central axis of the pipe; and three distinct flow conditions were assumed: upward flows with and without the effect of gravity and a downward flow. The numerical simulations showed good results when compared to experimental data.

PARSI et al. (2016) performed numerical simulations of two-phase flows with high air and water flow rates in a vertical pipe with an elbow at the top of the pipe and with an inner diameter of 76.2 [mm] throughout the pipe. The flow patterns captured in the simulations were churn and the transition between churn and annular flows. The superficial air velocities ranging from 10.3 - 33.9 [m/s] and two superficial water velocities equal to 0.3 and 0.79 [m/s] were considered during the simulations. The simulations were performed using the commercial ANSYS FLUENT 15 software. A hybrid method using a Eulerian approximation coupled with

the volume of fluid method was applied to solve the governing equations. The authors performed a qualitative and quantitative comparison between the numerical and experimental results. It was found that the numerical simulations were capable to capture different physical scenarios that were observed in the experiments and, in general, the numerical results showed a good agreement with the experimental data.

ALVES et al. (2017) studied the transient behavior of two-phase gas-liquid flows with high gas fractions in vertical pipes. The churn and annular flow patterns and the transition between them were analyzed experimentally and numerically in this study. In the experimental study, a vertical pipe with 42 [m] long and 49 [mm] in internal diameter was used. Figure 4 schematically illustrates the test facility used in these experiments. In the numerical study the authors developed an algorithm using the three-field formulation to solve the hyperbolic balance of mass, momentum and entropy equations for both fluids. The algorithm developed by the authors presented an absolute mean deviation of 14.5% for the pressure and 7.9% for the void fraction when compared with the experimental data.

TEKAVČIČ, KONČAR and KLJENAK (2019) performed three-dimensional numerical simulations of air-water churn flows in vertical pipes with 19 and 32 [mm] in internal diameter and 0.13 [m] long. This study aimed to investigate the frequencies of high amplitude periodic liquid waves present in this type of flow. The interFoam algorithm, present in the OpenFoam software, was used to perform these simulations. The interface compression method was used to describe the interface between the two phases and a study regarding the interface compression level was also performed. The numerical results showed a good qualitative and quantitative agreement when compared to the experimental data.

ADAZE, BADR and AL-SARKHI (2019) performed numerical simulations of annular air-water flows to study the onset of liquid film flow reversal phenomenon adjacent to the pipe wall. A vertical pipe with 76.2 [mm] in diameter and 3 [m] long was used in this study. The ANSYS Fluent 16.1 software was used to perform numerical simulations. The two-fluid method was employed to solve the problem. In the study of the liquid film flow reversal phenomenon, certain liquid flows were fixed and, for each of these, the gas flow was varied until the reversal of the liquid film was observed. The numerical results obtained in this study presented a good agreement when compared with experimental data present in the literature.

# 3 NUMERICAL METHODOLOGY

The study of fluid kinematics, in fluid dynamics, seeks to understand how the fluid flow occurs and how to describe its movements. For this purpose, there are two approaches typically used to describe the movement of a fluid. The first is called the Lagrangian method. In this method the path of an object (or a fluid particle) is followed individually. Newton's laws are used to describe the motion of this object and thus it is possible to accurately predict its displacement and the energy exchange involved during the process. The Lagrangian method tracks the position, velocity and other properties of each fluid particle individually (CENGEL and CIMBALA, 2014).

For fluid flows the Langrangian method may present some problems. Identifying and defining fluid particles as they move is a complicated task to accomplish. In addition, fluid particles continuously deform as they move within the flow. From a macroscopic point of view, the fluid is a continuum, so interactions between fluid particles are not easily described. From a microscopic point of view, a fluid is made up of billions of molecules that are continually colliding with each other. With these observations, it is noted that the use of the Lagrangian method is quite complicated for several practical applications (CENGEL and CIMBALA, 2014).

The second approach to describe the motion of a fluid is called the Eulerian method. In this methodology a control volume is defined in which fluid flows in and out. Instead of tracking individual particles of a fluid; field variables, space and time functions are defined within the control volume. The field variable at a given location and in an instant of time is the value of the variable for whatever fluid particle occupies that location at that time. In the Eulerian approach there is no interest in what happens to each individual fluid particle, but rather what happens to the field variables, regardless of which fluid particle is in the location of interest at that instant of time. The Eulerian method is usually more conventional than the Lagrangian method for fluid dynamics (CENGEL and CIMBALA, 2014).

For the resolution of two-phase flows usually two numerical methodologies are applied. The first method is a Eulerian-Lagrangian approach, where the continuous phase is

treated in the Eulerian approach and the dispersed phase with a Lagrangian approach. The motion of discrete particles is described by solving Newton's equations. The particle trajectories are calculated at the control volume. In segregated flows this approach is interesting to capture the interface between the two phases. Among the Eulerian-Lagrangian numerical methods available in the literature for the simulations of two-phase flows, the volume of fluid method is the most used.

The second method is a Eulerian-Eulerian approach, where the two phases are treated as a continuous medium interpenetrating each other and are solved through macroscopic conservation equations, which are valid throughout the flow domain. One of the numerical methods commonly used for two-phase flow simulations using this approach is the two-fluid model. This method is usually applied for dispersed flows and normally the discrete features of the dispersed phase are lost due to the averaging process. To overcome this problem, closure relationships are employed for mass, momentum and energy transfer at the interface between the two phases.

The applicability and quality of the results of each of the models described above strongly depend on the nature of the problem. The volume of fluid method is commonly used in problems where interface tracking is crucial, such as segregated flows, and the two-fluid model is employed when the interface scale length is smaller than the grid size, such as in dispersed flows.

The present work performed annular flow simulations. This type of flow has both segregated features, such as the well-defined division between the liquid film adjacent to the pipe wall and the gas core in the central region of the pipe, as well as dispersed features, such as the liquid droplets entrained in the gas core. To simulate this type of flow it would be interesting to combine the characteristics of the two methods mentioned previously. The OpenFoam presents in its library a hybrid algorithm that coupled the volume of fluid method and the two-fluid model to simulate multiphase flows. This algorithm is called multiphaseEulerFoam and was used in the simulations performed in this work.

## 3.1 OpenFoam

For the numerical simulations of the present work the OpenFoam software was used. This software was developed for the numerical analysis of continuum mechanics problems, with a strong application in Computational Fluid Dynamics (CFD). This program is free licensed and open source and was developed in the C ++ programming language. Its library consists of more than 100 algorithms, which were developed for specific applications (GREENSHIELDS, 2019).

MultiphaseEulerFoam is a hybrid algorithm present in the OpenFoam library, which was used in the numerical simulations of the present work. This algorithm was developed through the coupling of the two-fluid model and the volume of fluid method. The following subtopics describe the main mathematical equations implemented in this algorithm.

## 3.2 Governing Equations

In order to derive the mass and momentum conservation equations for the numerical model, the phases present in each computational cell must be distinguished to account the contributions of each phase present within it. A phase indicator function, Equation 11, is used to flag the algorithm whether or not a particular phase is present within the computational cell. If the phase of interest is present inside the cell, the conservation equations of this phase are multiplied by 1, otherwise they are multiplied by 0 and the equations for this phase are disregarded. In cells where more than one phase is present, the flow properties are obtained through an average process using the volume fraction as weighted parameter (CERNE, PETELIN and TISEL, 2001).

$$I_k(x,t) = \begin{cases} 1, & if\ (x,t)\ is\ in\ phase\ k \\ 0, & if\ (x,t)\ isn't\ in\ phase\ k \end{cases} \tag{11}$$

Equations 12 and 13 represent the mass and momentum conservation equations for each of the phases of an incompressible, isothermal multiphase flow with no mass transfer between phases.

$$\frac{\partial \alpha_k}{\partial t} + \vec{U}_k \cdot \nabla \alpha_k = 0 \tag{12}$$

$$\frac{\partial (\rho_k \alpha_k \vec{U}_k)}{\partial t} + (\rho_k \alpha_k \vec{U}_k \cdot \nabla)\vec{U}_k = \nabla \cdot [(\mu_k + \mu_t)\alpha_k \nabla \vec{U}_k] - \alpha_k \nabla \mathrm{P} + \rho_k \alpha_k \vec{g} + \vec{F}_{D,k} + \vec{F}_{s,k} \tag{13}$$

In Equation 13, from left to right, the first and second terms of this equation, left side, represent the temporal derivative and the momentum convection, respectively. The third term represents the momentum diffusion and the last four terms refer to field and surface forces. The terms $\vec{F}_{D,k}$ e $\vec{F}_{s,k}$ represent the interfacial forces, where the first term is the drag force and the second term is the surface tension force. Generally, in two-phase gas-liquid flows the interfacial forces are divided into two categories: drag force and non-drag force. The non-drag forces are the lift forces, virtual mass, turbulent dispersion and wall lubrication. In annular flows the drag forces are dominant and, therefore, the non-drag forces can be neglected (WARDLE and WELLER, 2013).

## 3.3 Surface Tension

Surface tension modeling ($\vec{F}_{s,k}$) is based on BRACKBILL, KOTHE and ZEMACH (1992). In this model the surface tension at the gas-liquid interface generates an additional pressure gradient, which is evaluated using a continuous surface force model. The surface tension is defined by Equation 14.

$$\vec{F}_{s,k} = \sigma \kappa \nabla \alpha \tag{14}$$

Where $\sigma$ is the surface tension coefficient between the fluids present in the flow and $\kappa$ is the local surface curvature, which is defined by Equation 15.

$$\kappa = -\nabla \cdot \left(\frac{\nabla \alpha}{|\nabla \alpha|}\right) \tag{15}$$

From Equations 14 and 15 it is possible to observe the need to obtain a good accuracy in the phase fraction distribution calculations for the proper evaluation of the surface curvature, which is necessary to describe the surface tension force and the corresponding pressure gradient across the free surface (TOCCI, 2016).

## 3.4 Drag Force

The interfacial drag force is represented by the resistance of the relative motion between the phases in a multiphase flow. In annular flows the size of the liquid droplets entrained in the gas core and the relative velocity between the phases are the main parameters that influence the magnitude of the drag force (TOCCI, 2016; WARDLE and WELLER, 2013). The drag force ($\vec{F}_{D,k}$) is defined by Equation 16.

$$\vec{F}_{D,k} = \frac{3}{4}\rho_c \alpha_c \alpha_d C_D \frac{\left|\vec{U}_d - \vec{U}_c\right|\left(\vec{U}_d - \vec{U}_c\right)}{d_d} = \alpha_c \alpha_d K\left(\vec{U}_d - \vec{U}_c\right) \tag{16}$$

Where the subscripts $c$ and $d$ denote the continuous and dispersed phases, respectively, and $K$ is given by Equation 17.

$$K = \frac{3}{4}\rho_c C_D \frac{\left|\vec{U}_d - \vec{U}_c\right|}{d_d} \tag{17}$$

The constant $C_D$ is called the drag coefficient and is usually obtained through experiments. However, if this is not possible, there are several empirical models in the literature to determine this coefficient taking into account different flow conditions. The OpenFoam has some empirical relationships in its library that are commonly used in multiphase flows. Schiller and Naumann's model (SCHILLER and NAUMANN, 1935),

Equation 18, is present in the software library and was used in the simulations of this work to determine the drag coefficient. This model was developed for two-phase laminar flows, which considers that one of the fluids is in the form of spherical droplets (water) dispersed inside a continuous medium (air). However, this model has been applied in several works in the literature for transient two-phase turbulent flows in vertical and horizontal pipe, including in TOCCI (2016), and, therefore, it has chosen to use it in the present work.

$$C_D = \begin{cases} \dfrac{24(1 + 0{,}15Re^{0{,}683})}{Re} & ;\ Re \leq 1000 \\ 0{,}44 & ;\ Re\ \geq 1000 \end{cases} \tag{18}$$

$$Re = \frac{\left|\vec{U}_d - \vec{U}_c\right| d_d}{\nu_c} \tag{19}$$

Where $\nu_c$, $d_d$ and $Re$ are the kinematic viscosity of the continuous phase, the diameter of the dispersed phase droplets and the Reynolds number, respectively.

The calculation of the drag coefficient in the solver can be performed by specifying a dispersed phase or by independent calculations considering each phase as the dispersed phase and the final drag coefficient, which is applied to the momentum conservation equations, is obtained by averaging these two values using the volume fraction as weighted parameter. This last method is known as blended scheme and was applied in the simulations performed in (WARDLE and WELLER, 2013).

## 3.5 Interface Capturing

To calculate the flow properties at the interface between phases, the interface compression method was used, which is an interface capture method. This method is not as accurate as other interface reconstruction methods, but it is much easier to implement, respects mass conservation and provides satisfactory results. This formulation adds an artificial compression term to mass conservation equations, as described by Equation 20 (WARDLE and WELLER, 2013).

$$\frac{\partial \alpha_k}{\partial t} + \vec{U}_k \cdot \nabla \alpha_k + \nabla \cdot (\vec{U}_c \alpha_k (1 - \alpha_k)) = 0 \quad (20)$$

The term $\alpha_k(1 - \alpha_k)$ ensures that this equation is only valid at the interface between the two phases, because in this region there is a mixture of the two phases and therefore $0 < \alpha_k < 1$. The velocity $\vec{U}_c$ is the artificial interface compression velocity defined by Equation 21, which is applied in the normal direction to the interface to compress the volume fraction field and maintain the interface description.

$$\vec{U}_c = C_\alpha |\vec{U}| \frac{\nabla \alpha}{|\nabla \alpha|} \quad (21)$$

Where $\frac{\nabla \alpha}{|\nabla \alpha|}$ is the unit vector normal to the interface for the direction of the applied compression velocity and $\vec{U}$ is the local velocity.

The interface compression coefficient $C_\alpha$ is the main way of controlling whether or not to use the interface compression method. In the algorithm the coefficient $C_\alpha$ is treated as a binary coefficient, which can assume the values 0 or 1. When $C_\alpha$ is equals to 0, for a given phase pair, it is imposed to the algorithm that does not use the interface compression method, that is, this phase pair is treated as dispersed phases and is modeled using the two-fluid model. For the case where $C_\alpha$ is equals to 1, the algorithm uses the interface compression method to capture the interface between the two phases. The implementation of this method in the solver is configured such that $C_\alpha$ is independently defined and applied for each phase pair present in the flow (TOCCI, 2016; WARDLE and WELLER, 2013).

## 3.6 Turbulence

Due to the turbulent nature of this type of flow, a turbulence model must be used. Considering the transient nature of the phenomenon and the high computational costs of CFD simulation the URANS (Unstady Reynolds-Averaged Navier-Stokes equations) $k - \omega\, SST$ model is selected in the OpenFoam library. This model is a combination between the $k - \epsilon$

and $k-\omega$ turbulence models. To calculate the turbulence at the pipe wall, the software checks the Reynolds number for each time step in the control volumes in this region and verifies which approach is more appropriate, low-Reynolds or law of the wall, and then the most appropriate method is employed for calculating the turbulence.

The $k-\epsilon$ and $k-\omega$ models are composed of two transport equations, one to solve the turbulent kinetic energy and the other one to solve the specific turbulent dissipation rate. The $k-\epsilon$ model presents better results for the free flow simulations and, therefore, is used to solve the computational domain that is far from the pipe walls. The $k-\omega$ model presents better results for the regions near a surface and, therefore, is used to solve the computational domain near the pipe walls.

The mathematical modeling that describes the $k-\omega\ SST$ turbulence model is presented along this subsection. All equations presented here were taken from MENTER, KUNTZ and LANGTRY (2003). The turbulent kinetic energy and the specific turbulent dissipation rate transport equations are defined by Equations 22 and 23, respectively. The $k-\epsilon$ and $k-\omega$ models are related through Equation 24.

$$\frac{\partial(\rho k)}{\partial t}+\frac{\partial(\rho\vec{U}_i k)}{\partial x_i}=\tilde{P}_k-\beta^*\rho k\omega+\frac{\partial}{\partial x_i}\left[(\mu+\sigma_k\mu_t)\frac{\partial k}{\partial x_i}\right] \tag{22}$$

$$\frac{\partial(\rho\omega)}{\partial t}+\frac{\partial(\rho\vec{U}_i\omega)}{\partial x_i}=\alpha\rho S^2-\beta\rho\omega^2+\frac{\partial}{\partial x_I}\left[(\mu+\sigma_\omega\mu_T)\frac{\partial\omega}{\partial x_i}\right]+2(1-F_1)\rho\sigma_{w2}\frac{1}{\omega}\frac{\partial k}{\partial x_i}\frac{\partial\omega}{\partial x_i} \tag{23}$$

$$\varepsilon=\beta^*\omega k \tag{24}$$

In Equation 22, from left to right, the first and second terms of this equation, left side, refer to the temporal derivative and the turbulent kinetic energy convection, respectively. The third, fourth and fifth terms of this equation, right side, refer to the production, dissipation and diffusion of turbulent kinetic energy. The terms of Equation 23 have an analogous meaning to Equation 22, but now the specific turbulent dissipation rate is considered. However, in the latter equation, an additional term arises. In this new term $F_1$ represents the coupling function between the $k-\epsilon$ and $k-\omega$ turbulence models and is defined by Equation 25. This function is responsible for the smooth transition between these two models.

$$F_1 = tanh\left\{\left\{min\left[max\left(\frac{\sqrt{k}}{\beta^* \omega y}, \frac{500\nu}{y^2 \omega}\right), \frac{4\rho\sigma_{\omega 2} k}{CD_{k\omega} y^2}\right]\right\}^4\right\} \quad (25)$$

$$CD_{kw} = max\left(2\rho\sigma_{\omega 2}\frac{1}{\omega}\frac{\partial k}{\partial x_i}\frac{\partial \omega}{\partial x_i}, 10^{-10}\right) \quad (26)$$

Where $k$, $\omega$, and $y$ are the turbulent kinetic energy, the specific turbulent dissipation rate and the distance from the mesh cell to the nearest wall in the computational domain, respectively. The terms $k$ and $\omega$ are mathematically defined in section 4.2 of this work. The other terms that have not been presented throughout the work are constant and are presented in Table 1.

For regions far from the pipe wall the term $F_1$ is equal to 0 and the flow is solved by the $k - \varepsilon$ model. For regions near the pipe wall the term $F_1$ is equal to 1 and the flow is solved by the $k - \omega$ model. For an intermediate region the term $F_1$ is a value between 0 and 1 allowing a smooth transition between these two models. The turbulent viscosity ($\nu_t$) is defined by Equation 27. This term is responsible for connecting the conservation equations, Equations 12 and 13, with the turbulence model.

$$\nu_t = \frac{a_1 k}{\max(a_1\omega, SF_2)} \quad (27)$$

Where $S$ is the invariant measure of the strain rate and $F_2$ is a second coupling function which is defined by Equation 28.

$$F_2 = tanh\left[\left[max\left(\frac{2\sqrt{k}}{\beta^* \omega y}, \frac{500\nu}{y^2 \omega}\right)\right]^2\right] \quad (28)$$

A production limiter is used in the $k - \omega\ SST$ model to prevent the occurrence of turbulence in stagnation regions, as defined by Equation 29.

$$\tilde{P}_k = \mu_t \frac{\partial \vec{U}_i}{\partial x_j}\left(\frac{\partial \vec{U}_i}{\partial x_j} + \frac{\partial \vec{U}_j}{\partial x_i}\right) \rightarrow \tilde{P}_k = \min(\tilde{P}_k, 10\beta^* \rho k \omega) \quad (29)$$

The $F_1$ function is also used to couple the empirical constants of the $k-\epsilon$ and $k-\omega$ turbulence models, as described by Equation 30.

$$\alpha = \alpha_1 F_1 + \alpha_2 (1 - F_1) \tag{30}$$

The empirical constants of these two turbulence models are presented in Table 1.

Table 1 - Turbulence model constants $k-\epsilon$ e $k-\omega$.

| $\boldsymbol{k-\omega}$ | $\boldsymbol{k-\epsilon}$ |
|---|---|
| $\beta^* = 0{,}09$ | $\beta^* = 0{,}09$ |
| $\alpha_1 = \frac{5}{9}$ | $\alpha_2 = 0{,}44$ |
| $\beta_1 = \frac{3}{40}$ | $\beta_2 = 0{,}0828$ |
| $\sigma_{k1} = 0{,}85$ | $\sigma_{k2} = 1$ |
| $\sigma_{\omega 1} = 0{,}5$ | $\sigma_{\omega 2} = 0{,}856$ |

Source: MENTER, KUNTZ e LANGTRY (2003).

## 3.7 Courant Number

The Courant number is a dimensionless quantity that represents the advective flow through the computational mesh cells over a given time interval. Its mathematical definition is given by Equation 31.

$$C_O = \Delta t \sum_{i=1}^{n} \frac{\vec{U}_i}{\Delta x_i} \tag{31}$$

Where $\Delta t$ and $\Delta x$ are the time step and spacing of mesh cells, respectively.

The Courant-Friedrichs-Lewy condition (CFL condition) is a necessary condition for the solution convergence of certain partial differential equations through numerical methods that require explicit temporal integration. This condition imposes a limit value for the Courant

number, which can be controlled by variations in computational mesh spacing, time step or flow velocity. If the Courant number is greater than the limit value stipulated by the numerical methodology employed in the simulations, the numerical solutions may produce incorrect results (COURANT, FRIEDRICHS and LEWY, 1928).

## 3.8 Solution Procedure

WARDLE and WELLER (2013) briefly described the multiphaseEulerFoam solver solution procedure, as illustrated in Figure 7. This solver was used in the numerical simulations of the present work.

Figure 7 – MultiphaseEulerFoam schematic solution procedure.

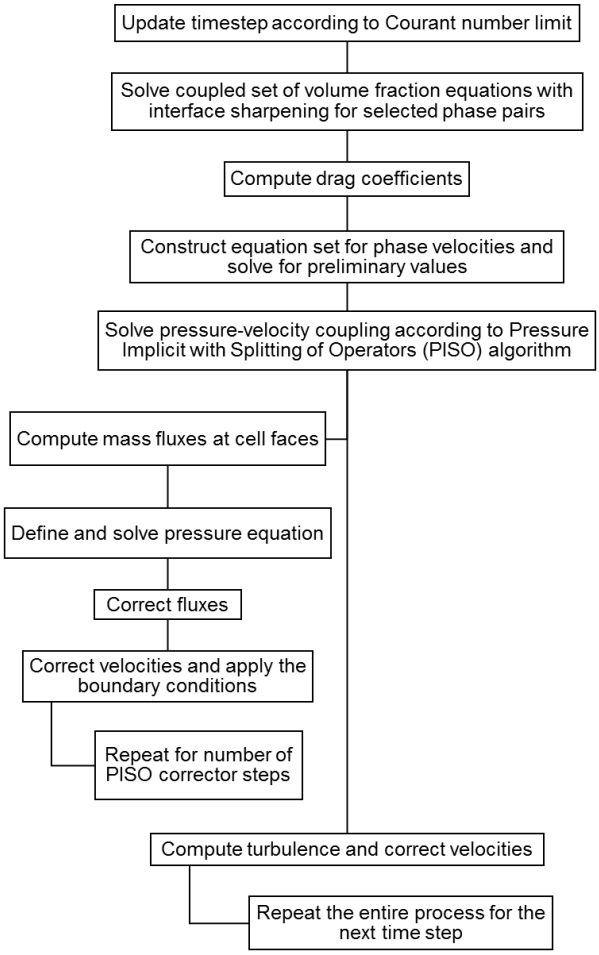


Source: Author (2020).

# 4 NUMERICAL SIMULATIONS CHARACTERISTICS

This work aims to numerically simulate transient, turbulent and isothermal annular air-water flows in a vertical pipe. The mathematical modeling of this problem was presented in section 3. In order to simplify the numerical calculations and decrease the computational time to perform the simulations, the following assumptions were adopted:

- Incompressible flow (for both fluids);
- Two-phase flow with non-reactive fluids;
- Constant fluid properties throughout the flow.

In this section the numerical aspects and some physical properties of the fluids necessary to perform the simulations were presented.

## 4.1 Fluid Properties

Among the several properties of a fluid, the most relevant for annular two-phase flow simulations are the specific mass, dynamic and kinematic viscosities of the fluids present in the flow and the surface tension coefficient between the two phases. These properties were obtained at 25 [ºC] and 2.38 [bars], which were the inlet conditions used in WOLF, JAYANTI and HEWITT (2001).

The water specific mass (liquid phase) is constant in relation to pressure variation, so it was obtained directly from tables present in ÇENGEL and CIMBALA (2014). The air (gas phase) was assumed to be a perfect gas. The ideal gas law, Equation 32, was applied to obtain its specific mass at a pressure of 2,38 [bars].

$$PV = nRT \tag{32}$$

$$\rho = \frac{m}{V} \tag{33}$$

$$n = \frac{m}{M} \tag{34}$$

Where $n$, $R$, $T$ and $M$ are the number of moles, the universal perfect gas constant $\left(8{,}31\ \left[\frac{J}{K.mol}\right]\right)$, the temperature and the molar mass, respectively. By substituting Equations 33 and 34 in Equation 32, it is possible to determine the air specific mass according to Equation 35.

$$\rho = \frac{PM}{RT} \tag{35}$$

The dynamic viscosity of Newtonian fluids, in general, has a strong influence on temperature, but a low dependence on pressure. According to BIRD, STEWART and LIGHTFOOT (2002), low density fluids, such as air, have a pressure-independent dynamic viscosity for pressures up to 10 [atm] at temperatures above their critical temperature. The critical air temperature is 132.5 [K], as reported in CENGEL and CIMBALA (2014). Therefore, the dynamic air viscosity under ambient conditions can be used.

The fluid kinematic viscosity can be obtained by Equation 36.

$$\nu = \frac{\mu}{\rho} \tag{36}$$

Where $\mu$ is the fluid dynamic viscosity. Table 2 presents the air and water properties used in the simulations of the present work. The surface tension coefficient between air and water used in the numerical simulations was 0.0742 [N/m] (PRAUSNITZ, LICHTENTHALER AND AZEVEDO, 1998).

Table 2 - Fluid properties used in the numerical simulations.

| | **Air** | **Water** |
|---|---|---|
| $\boldsymbol{\rho}\ [\boldsymbol{kg/m^3}]$ | 2,78 | 997 |
| $\boldsymbol{\mu}\ [\boldsymbol{Pa.s}]$ | $1{,}84 \times 10^{-5}$ | $1{,}000 \times 10^{-3}$ |
| $\boldsymbol{\nu}\ [\boldsymbol{m^2/s}]$ | $6{,}62 \times 10^{-6}$ | $1{,}003 \times 10^{-6}$ |

Source: Author (2020).

## 4.2 Boundary Conditions

The computational domain was divided into three parts: inlet, wall and outlet. The pipe inlet was divided into a central circular region, through which the air flows, and a ring that surrounds this central core, through which the water flows. This division into two subdomains at the pipe inlet was performed in order to impose an annular flow pattern at the inlet aiming to accelerate the convergence of the simulations. Figure 8 illustrates the geometry used in the simulations of this work and the subdivision at the pipe inlet. As can be seen in this figure, the simulations were performed in a pipe with 10.01 [m] and not 10.78 [m] long, because in this position was located the last pressure sensor, which is a crucial parameter for the boundary conditions at the pipe outlet.

For the velocity field, the air and water mass fluxes were prescribed at the pipe inlet. The no-slip condition was used at the pipe wall and the zero gradient boundary condition was applied at the pipe outlet. For the pressure field, a fixed mean pressure value was specified at the pipe outlet and at the pipe inlet and the wall the zero gradient boundary condition was used. The mass fluxes and pressure values prescribed in the boundary conditions were taken from WOLF, JAYANTI and HEWITT (2001).

The $k - \omega\ SST$ turbulence model used in the simulations also requires boundary conditions for turbulent kinetic energy and specific turbulent dissipation rate. At the pipe inlet, the turbulent kinetic energy was calculated for each fluid through Equations 37. At the pipe outlet, the zero gradient boundary condition was used. At the pipe wall, a wall function named *kqRWallFunction* in the OpenFoam software was used, which provides a pure zero-gradient boundary condition (LIU, 2017).

$$k = \frac{3}{2}\left(I\left|\vec{U}_{ref}\right|\right)^2 \quad (37)$$

Where $I$ is the turbulent intensity and $u_{ref}$ is the reference velocity, which is velocity of each fluid used in the boundary conditions at the pipe inlet. WOLF, JAYANTI and HEWITT (2001) did not present any data regarding turbulent properties in their work.

PARSI et al. (2016) used in their work, in which gas-liquid churn flows were simulated in a vertical pipe with an elbow at the top of the pipe, a turbulent intensity of 5%, which is the same value recommended by the ANSYS Fluent manual 15 (2013). These authors got good results in their simulations and, based on this work, it was decided to use in the present study the same turbulent intensity.

Figure 8 - Geometry used in the numerical simulations.

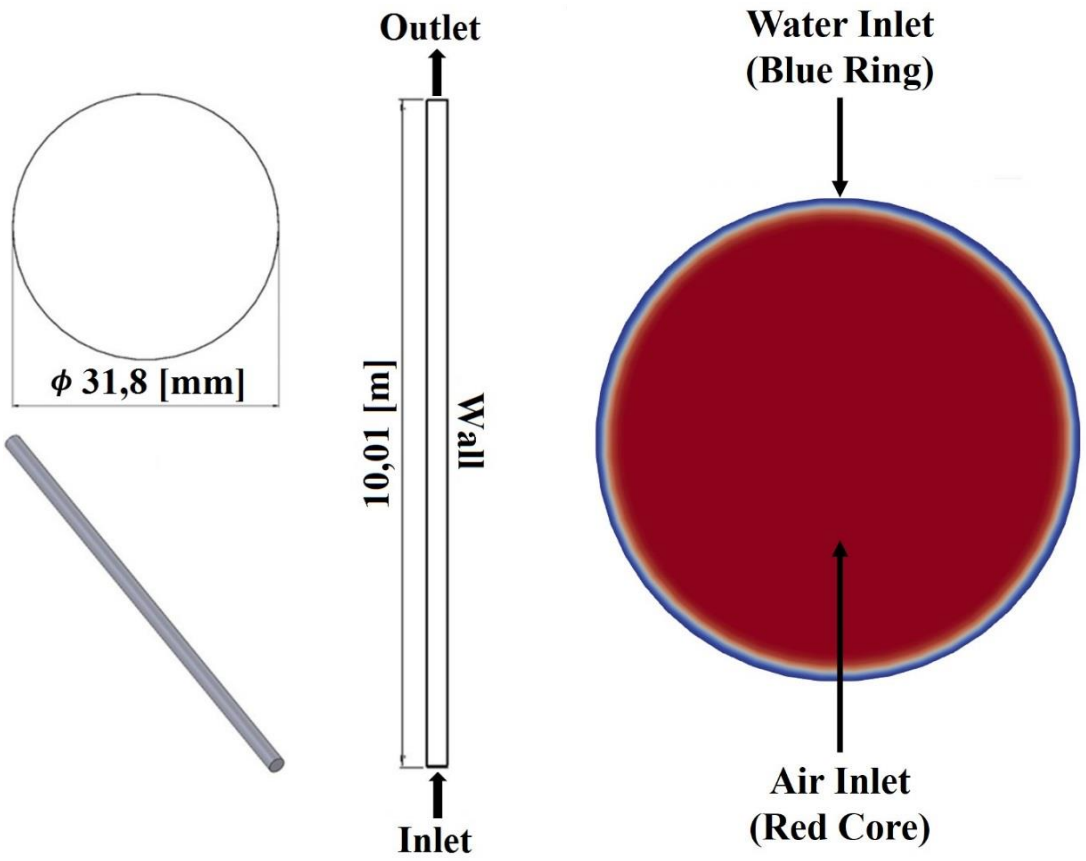


Source: Author (2020).

At the pipe inlet, the specific turbulent dissipation rate was calculated for each fluid through Equation 38. At the pipe outlet the zero gradient boundary condition was used.

$$\omega = \frac{k^{0,5}}{C_\mu^{\frac{1}{4}} \ell} \tag{38}$$

$$\ell = 0,07D \tag{39}$$

Where $C_\mu$ is a constant equal to 0,09 and $\ell$ is the turbulent scale length, defined by Equation 39 for cylindrical pipes. Equations 37 and 38 were taken from MATHIEU and SCOTT (2000).

At the pipe wall, a wall function named *omegaWallFunction* in the OpenFoam software was used for the specific turbulent dissipation rate calculation. This wall function can switch between viscous and logarithmic region, in the boundary layer, according to the position of $y^+$ (dimensionless distance from the wall, which is defined by Equation 40). In the intersection of the viscous sublayer and log-law region value is calculated through blending the viscous and log-law sublayer value. The specific turbulent dissipation rate in the viscous layer and in the log-law layer are defined by Equations 41 and 42, respectively (LIU, 2017).

$$y^+ = \frac{y u^*}{\upsilon} \tag{40}$$

$$\omega_{vis} = \frac{6\upsilon}{0,075 y^2} \tag{41}$$

$$\omega_{log} = \frac{k^{\frac{1}{2}}}{C_\mu^{\frac{1}{4}} k y} \tag{42}$$

Then, the specific turbulent dissipation rate is obtained by combining Equations 41 and 42.

$$\omega = \sqrt{\omega_{log} + \omega_{vis}} \tag{43}$$

Table 3 presents the boundary conditions for the cases studied in the section 5 of the present work. This table does not present the zero gradient, non-slip and wall function boundary conditions, as their applications were specified throughout the text.

Table 3 - Boundary conditions of the numerical simulations performed in this study.

| | | Cases 1 and 2 | Case 3 | Case 4 |
|---|---|---|---|---|
| Inlet | $\dot{m}_L$ [kg/s] | 0.0953 | 0.0476 | 0.0953 |
| | $\dot{m}_G$ [kg/s] | 0.0564 | 0.0564 | 0.0770 |
| | $k_L$ [m²/s²] | 1.68e-3 | 4.19e-4 | 1.68e-3 |
| | $k_G$ [m²/s²] | 3.635 | 3.635 | 6.784 |
| | $\omega_L$ [1/s] | 33.58 | 16.79 | 33.58 |
| | $\omega_G$ [1/s] | 1564 | 1564 | 2136 |
| Outlet | P [bar] | 1.724 | 1.827 | 1.552 |

Source: Author (2020).

### 4.3 Computational Mesh

PEREZ, ABDULKADIR AND AZZOPARDI (2011) studied the application of different mesh structures in two-phase gas-liquid flow simulations in cylindrical pipes. The authors found that different mesh topologies result in different numerical precisions. The mesh structure named “butterfly” by these authors, called “O-grid” by TOCCI (2016), presented the best results in terms of numerical accuracy. In this mesh structure, the central region of the pipe is described by a mesh in cartesian coordinates and a mesh in cylindrical coordinates surrounds this central region and extends to the pipe wall. This topology allows a mesh refinement near the pipe wall, which is of great interest for the study of multiphase flows.

The butterfly mesh topology was used by TOCCI (2016) in his study. This author wrote a script in OpenFoam for the generation of these type of mesh. In the present work, the same script and mesh topology were used for the numerical simulations performed here. Figure 9 illustrates the application of this mesh topology to a pipe cross-section of one of the cases discussed here. The mesh is formed by hexahedron elements, however in Figure 9 its

appearance is composed of triangular prismatic elements, which is an inconvenience that emerged in the post-processing software and that was not possible to fix.

Figure 9 - Butterfly mesh topology used in the numerical simulations.

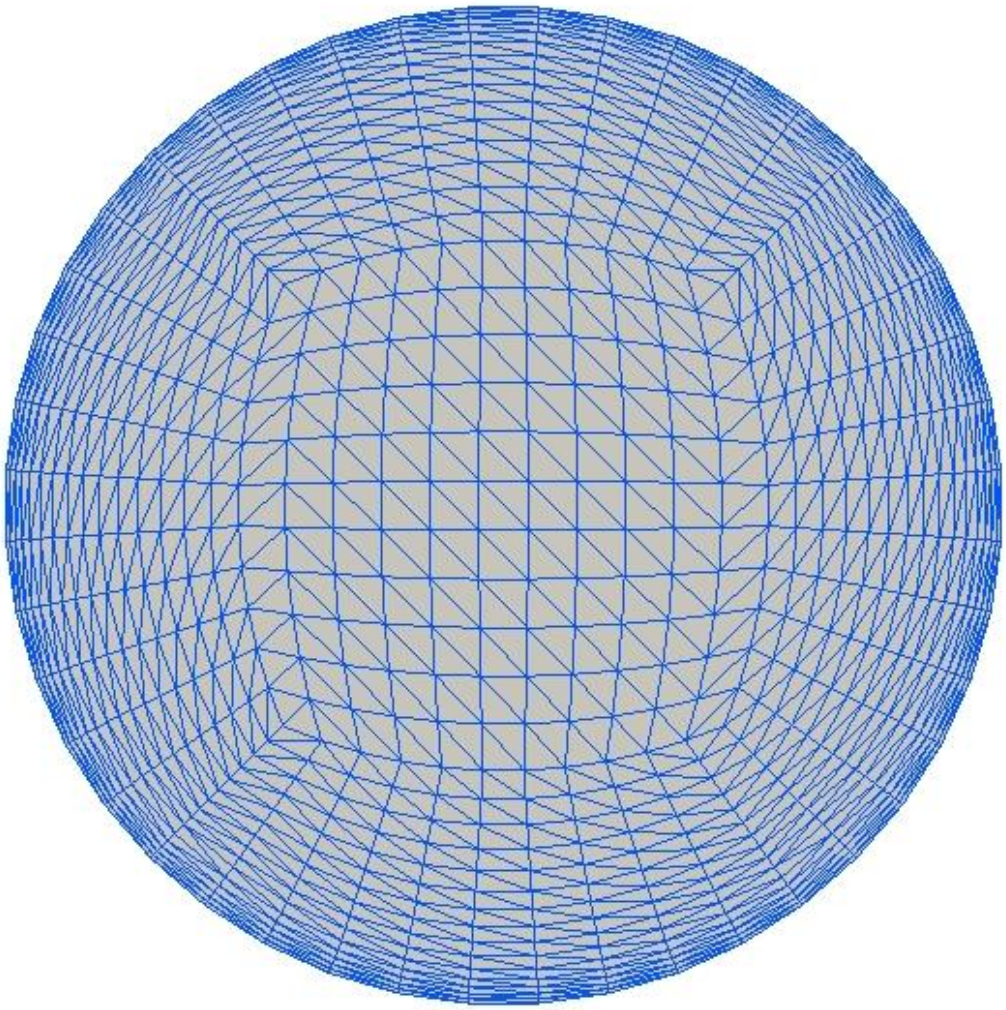

Source: Author (2020).

A mesh of 312400 volumes was used in all simulations performed in the present work. The number of cells along the longitudinal axis of the pipe (Z axis) is uniform. It was not possible to perform an appropriate mesh convergence study to check the mesh dependence in the simulations due to the high computational costs required to simulate flows of this nature. However, the numerical results were compared with experimental data to evaluate the accuracy of the simulations.

## 4.4 Solver Settings

The system subdirectory in OpenFoam contains all files related to the solution procedure. The computational domain was discretized using the cell centered finite volume method. The conservation equations were discretized in time and space to be numerically solved in a similar way to that presented in TOCCI (2016). The transient terms, gradients and Laplacians were discretized using implicit Euler, least squares and Gauss linear limited schemes, respectively. The divergent terms were separated in turbulent, phase fraction, convection and other terms, which were discretized using Gauss limitedLinear, vanLeer, Gauss limitedLinearV and linear Gauss schemes, respectively. The limitedLinear Gauss scheme uses a constraint function to avoid non-physical values that arise due to numerical errors. The vanLeer scheme is second order and has a constraint function similar to the previous one. The limitedLinearV scheme calculates a single limiting for all vector components. The linear interpolation was employed to obtain the flow properties on the cell faces. Finally, pressure-velocity coupling was performed using the PISO algorithm (GREENSHIELDS, 2018).

## 4.5 Surface Tension Correction

Version 7 of OpenFoam was used in the simulations of the present work. TOCCI (2016) used the version 2.2.x in his study and found that the surface tension was omitted in the velocity field reconstruction in the multiphaseEulerFoam algorithm. This same problem was also found in the current version and, therefore, before performing any numerical simulations, it was necessary to implement this line in the code. Figure 10 shows the part of the algorithm with the problem, where the seventh line was missing in the original code.

Figure 10 - Missing line in the original multiphaseEulerFoam algorithm.

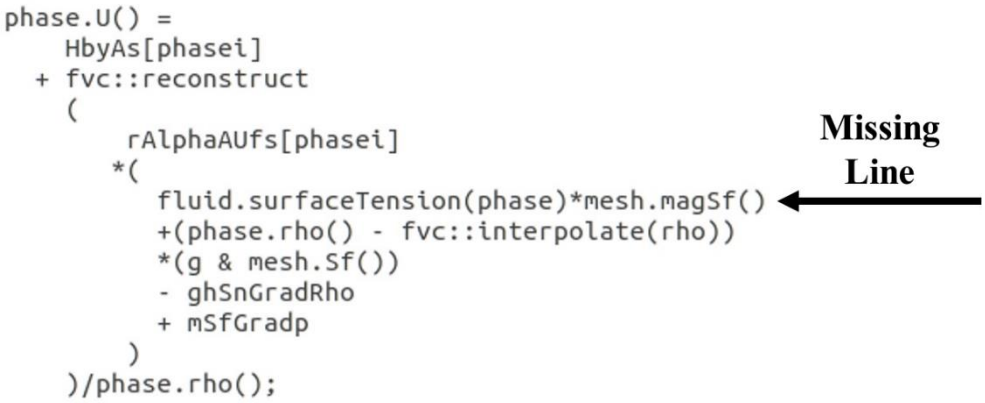


Source: Author (2020).

# 5 RESULTS AND DISCUSSION

This section presents the results of the numerical simulations performed in this work. All analysis performed in this section were made after the flows reached the steady state. A total of 4 simulations were performed, in which different air and liquid mass fluxes, Courant numbers and droplet diameters were tested.

## 5.1 Case 1

The first flow analyzed has air and liquid mass fluxes equal to 71 and 120 [kg/m².s], respectively. A droplet diameter for the dispersed phase and a Courant number equal to $50 \times 10^{-6}$ [m] and 0.25, respectively, were used in this simulation. These are the same values used in the 3D annular mixer model presented in WARDLE and WELLER (2013). The boundary conditions applied for this case were presented in the first column of Table 3.

Figure 11 shows the numerical results for the mean pressure variation as function of time for 7 planes along the pipe. Through this figure it is possible to observe that the maximum pressure occurs at the pipe inlet and decrease to its minimum value at the pipe outlet. This behavior was similar to that reported in the experiments of WOLF, JAYANTI and HEWITT (2001). The liquid film thickness decreases along the pipe, as illustrated by the increase of the void fraction in Figure 13, and, consequently, the flow accelerates causing this pressure drop.

Figure 12 shows a comparison between the experimental and numerical pressure in 7 planes along the pipe for the last two seconds (3 – 5 [s]) with differences up to 15%. Through this figure it is possible to observe that the average pressure in the cross sections obtained in the numerical simulations were underestimated in relation to the experimental results. The numerical pressure curve did not show a linear behavior as in the experimental one. This curve showed a significant slope change in approximately 1.5 [m] in relation to the pipe inlet, in the same region where the simulations began to present problems in capturing the liquid films, as shown in Figures 13 and 14. With the pulverization of the liquid film, substantial changes occur

in the velocity field, which consequently affects the pressure field and, therefore, causing this distinction in the behavior between the two curves.

Figure 11 - Mean pressure as function of time.

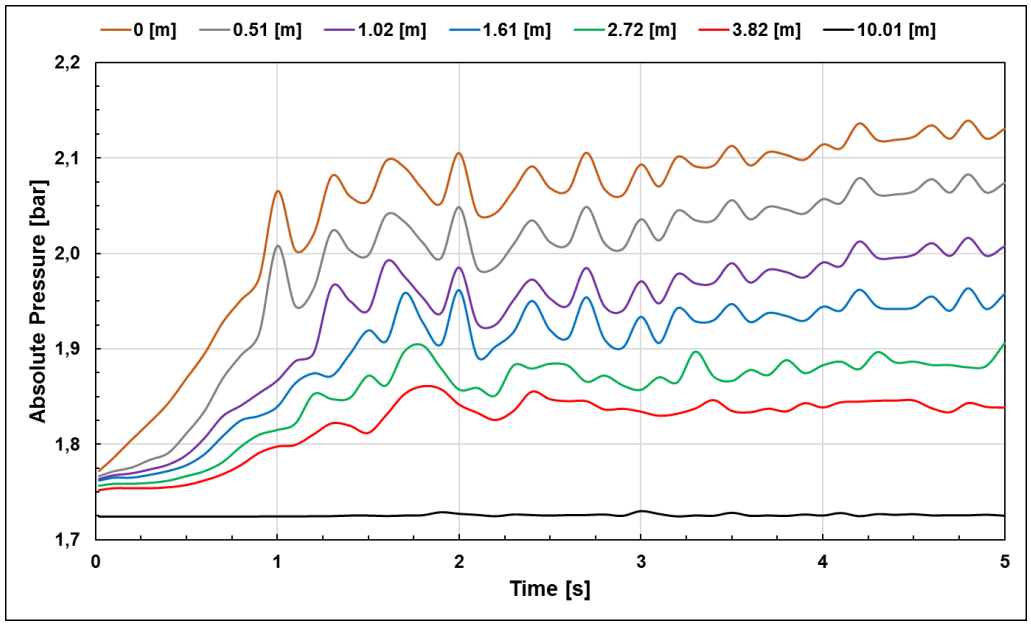


Source: Author (2020).

Figure 12 - Numerical and experimental mean pressure for the Case 1.

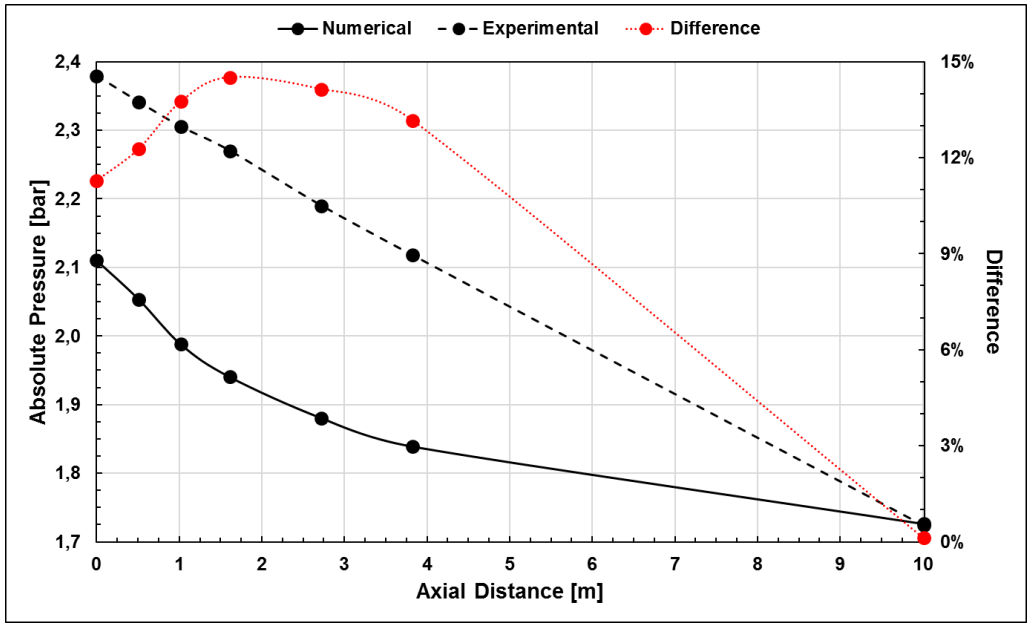


Source: Author (2020).

Figure 13 shows the variation of the mean void fraction (volumetric gas fraction) as function of time for 6 planes along the pipe.

Figure 13 - Mean void fraction as function of time for the Case 1.

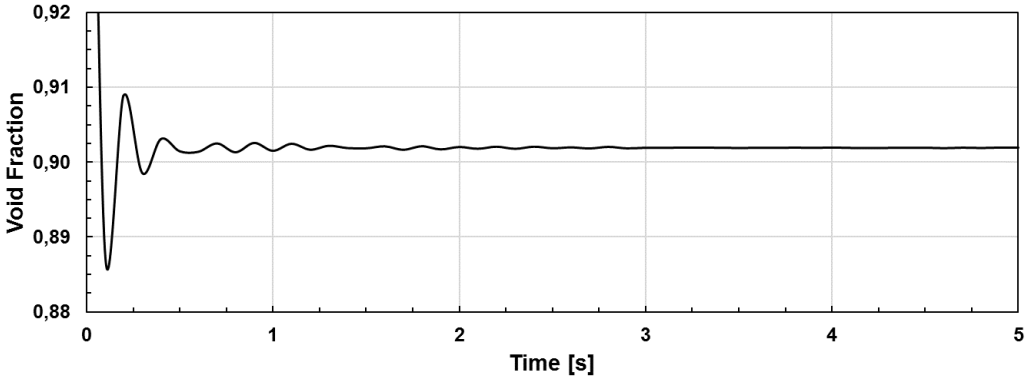


a) Plane positioned at 0,05 [m] from the inlet.

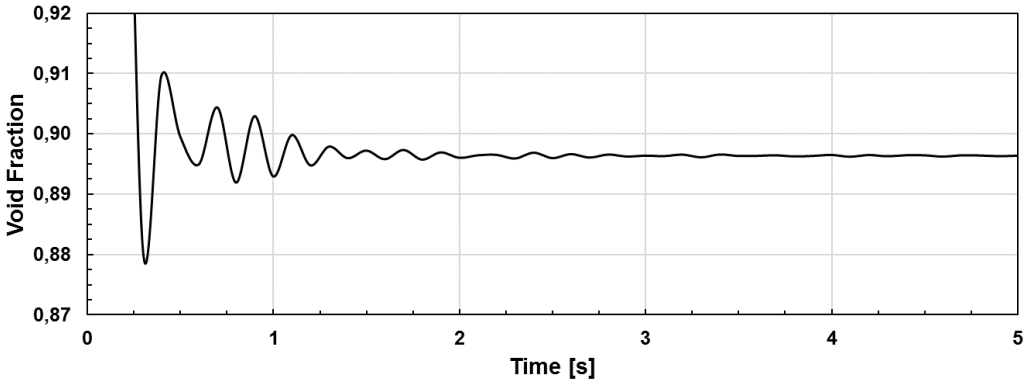


b) Plane positioned at 0,25 [m] from the inlet.

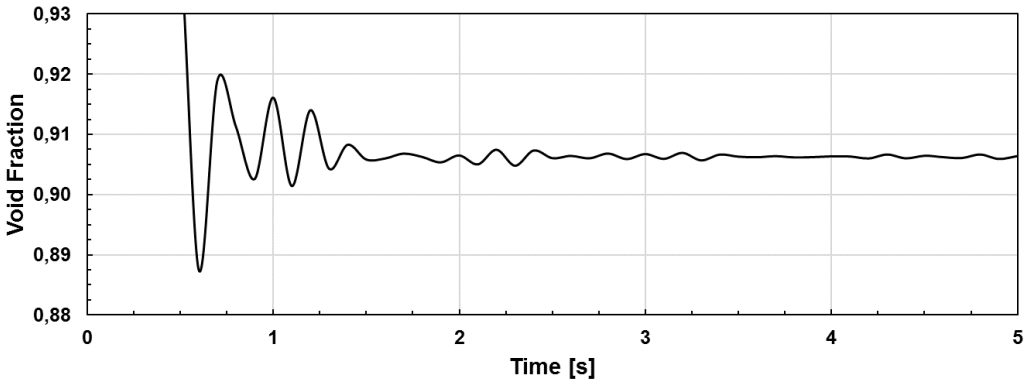


c) Plane positioned at 0,44 [m] from the inlet.

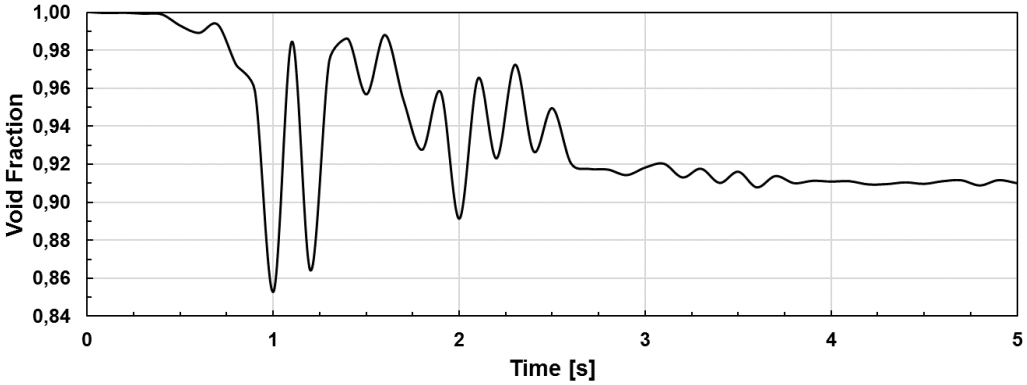


d) Plane positioned at 0,94 [m] from the inlet.

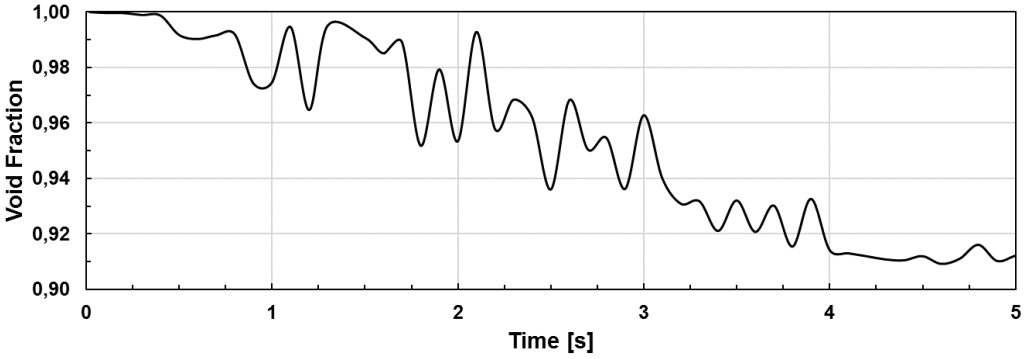


e) Plane positioned at 1,07 [m] from the inlet.

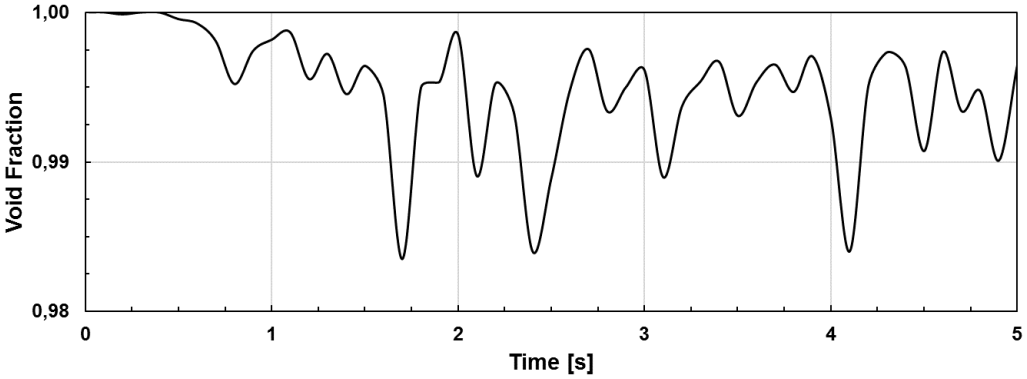


f) Plane positioned at 3,85 [m] from the inlet.

Source: Author (2020).

The void fractions in the first five planes, Figures 13.a) through 13.e), initially presented large oscillations, due to the arrival of the liquid flow in these regions, until they converged to a nearly constant value, indicating the complete formation of the liquid film.

After the convergence of the void fraction, small waves appear on the graphs, which represent the disturbance waves. It can also be observed that at 0.25 [m] the void fraction is smaller than at 0.05 [m], that is, the liquid film in the second plane is thicker than in the first one. This same behavior was also observed in WOLF, JAYANTI and HEWITT (2001), in which these authors stated that this was due to the transition from laminar to turbulent flow regime.

The void fraction in the last plane, Figure 13.f), showed an average value of approximately 99,5%. This means that almost all liquid film has been pulverized. However, in the experiments, it was found that only about 30% of the water mass flux of the liquid film was entrained in the gas core. Among the several factors that may have caused this inconsistency, it is strongly believed that this problem has arisen due to the inefficient capture of the interface between the two phases, resulting in an underestimated surface tension, which is unable to maintain the liquid film adjacent to the pipe wall. Unfortunately, it was not possible to cover all the suspicions that originated this anomalous behavior present in the numerical simulations due to the lack of computational resources.

Figure 14 shows the distribution of the water fraction in 6 cross-sections along the pipe for a numerical time equal to 5 [s].

Figure 14: Water fraction distribution in the cross-sections for the Case 1.

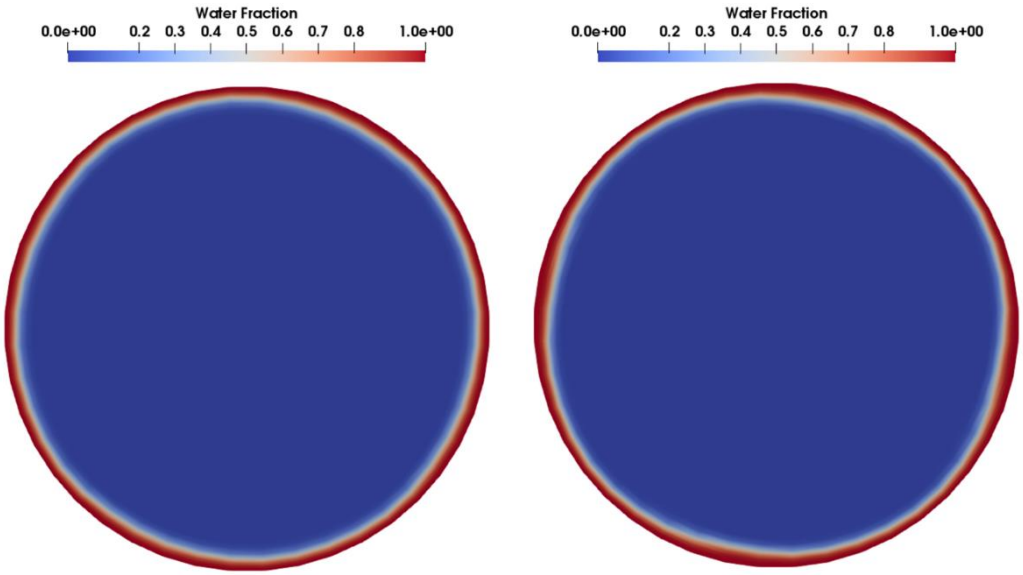


a) 0,05 [m] b) 0,25 [m]

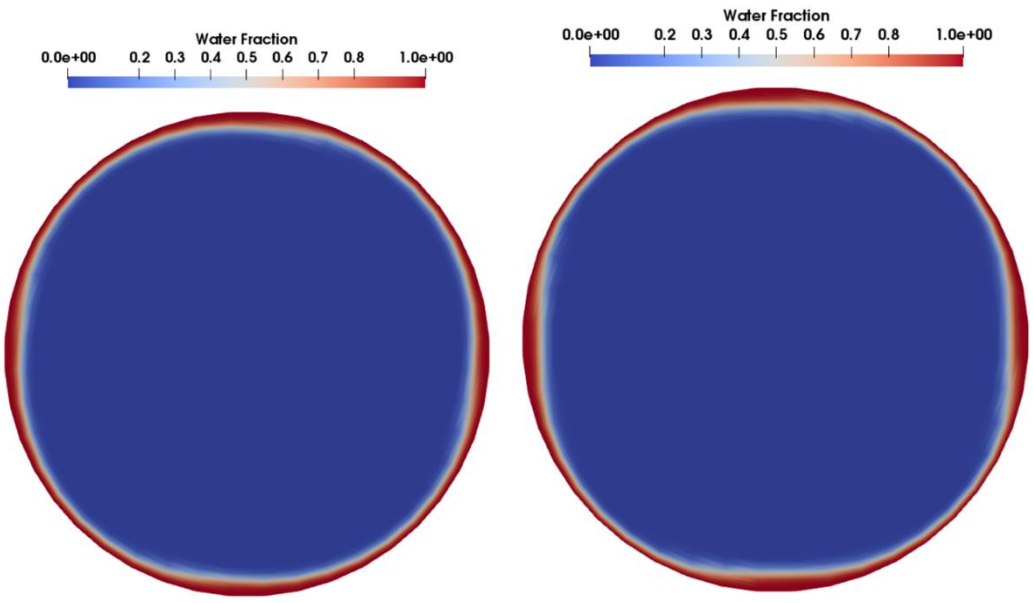


c) 0,44 [m] d) 0,94 [m]

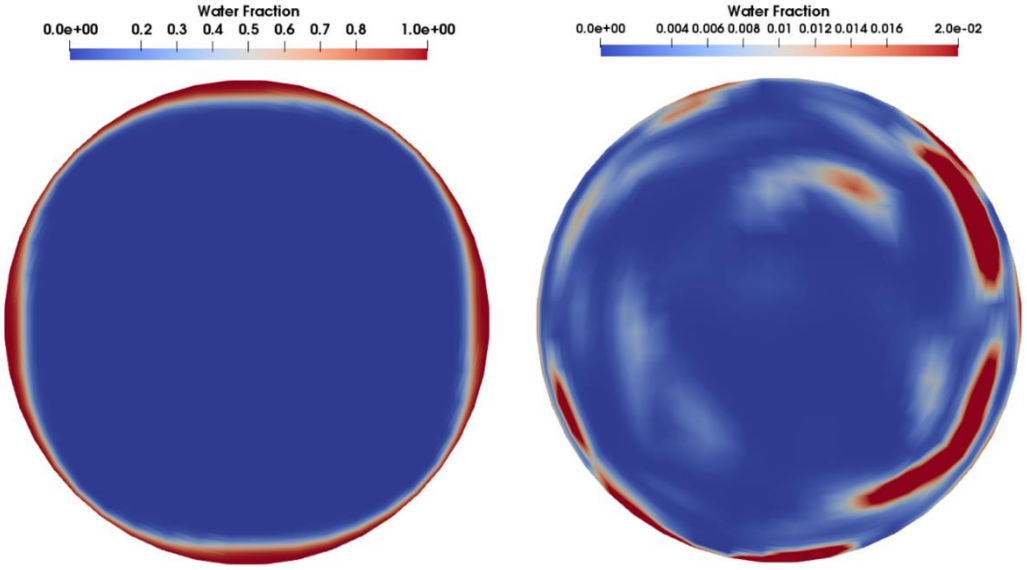


e) 1,07 [m] f) 3,85 [m]

Source: Author (2020).

As mentioned earlier, in the first five planes, Figures 14.a) through 14.e), the simulations were able to capture the liquid film. In the experiments, the thickness and the liquid

mass flux were provided in some positions along the pipe. In the numerical simulations, it is possible to calculate, approximately, the liquid film thickness using the volumetric water fraction through Equation 1. However, the volumetric water fractions in the simulations take into account both the entrained droplets and the liquid film and, therefore, this direct comparison overestimates the numerical liquid film thickness. To correct this problem an interpolation was necessary to compensate the water volume fraction of the entrained droplets. As the data for film thicknes and liquid film flow rate are obtained in different positions in the experimental data has to be interpolated between points. The first part was to obtain an equation for the rate of change of the liquid film flux using a simple regression in MS Excel. This equation is then used to compensate the numerical water volumetric fraction. If from one position to the other the liquid film flux decreases by some value, the fraction of water flowing in the form of droplets increases by the same amount.

Table 4 presents a comparison between the numerical and experimental liquid film thickness, where the numerical results were obtained by averaging the last second (4 – 5 [s]) of the simulation. In this table, it is possible to observe that the numerical liquid film thicknesses were overestimated in relation to the experimental ones. This difference can be corrected by calibrating some parameters of the numerical model, such as, for example, the dispersed phase diameter. In general, in the regions where the simulation was able to capture the liquid film, the numerical results were in agreement with the experimental ones.

Table 4 - Comparison between the numerical and experimental liquid film thickness for the Case 1.

| **Position** | **Liquid Film Thickness** | |
|---|---|---|
| | **Experimental** | **Numerical** |
| **[m]** | **[mm]** | **[mm]** |
| 0,05 | 0,551 | 0,793 |
| 0,25 | 0,610 | 0,821 |
| 0,44 | 0,572 | 0,724 |
| 0,94 | 0,467 | 0,657 |
| 1,07 | 0,465 | 0,631 |

Source: Author (2020).

In the last plane, Figure 14.f), a maximum water fraction scale equal to 2% was used. In this figure, it is possible to observe that there is a small percentage of liquid adjacent to the pipe wall flowing upwards. However, as previously mentioned, this is a physical inconsistency that appeared in the simulations, since there should be a consistent liquid film flowing upwards adjacent to the pipe wall.

Figure 15 shows the velocity distribution in 6 cross-sections along the pipe for a numerical time equal to 5 [s]. The velocity profiles in the first five planes, Figures 15.a) through 15.e), are well defined, where the lowest velocities occur in the liquid film and the highest velocities occur in the gas core. The first plane, Figure 15.a), presents a uniform velocity distribution in the gas core, because it is very close to the pipe inlet, where the boundary conditions were specified. The subsequent planes are farthest from the pipe inlet and, therefore, the velocity distribution in the gas core has a non-uniform profile, where the velocities increase radially towards the pipe center. In the last plane, Figure 15.f), the velocity profile is similar to that of a single-phase flow, since in this region almost all the liquid film has been pulverized and flows as entrained droplets in the gas core.

Figure 15 - Velocity distribution in the cross-sections for Case 1.

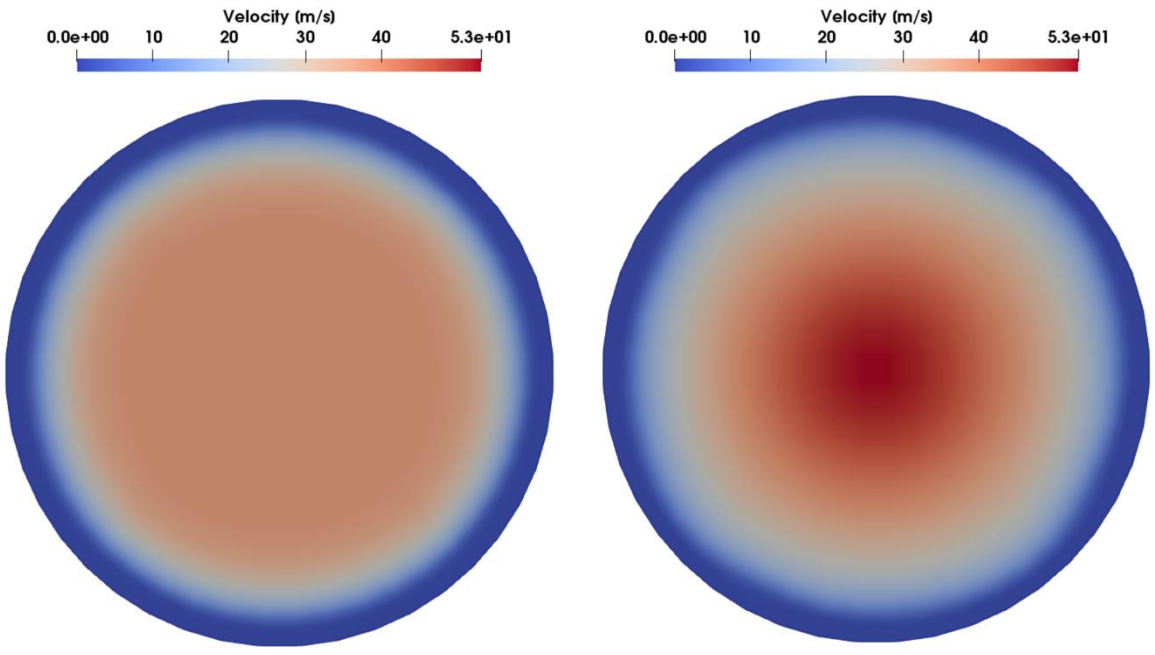


a) 0,05 [m] b) 0,25 [m]

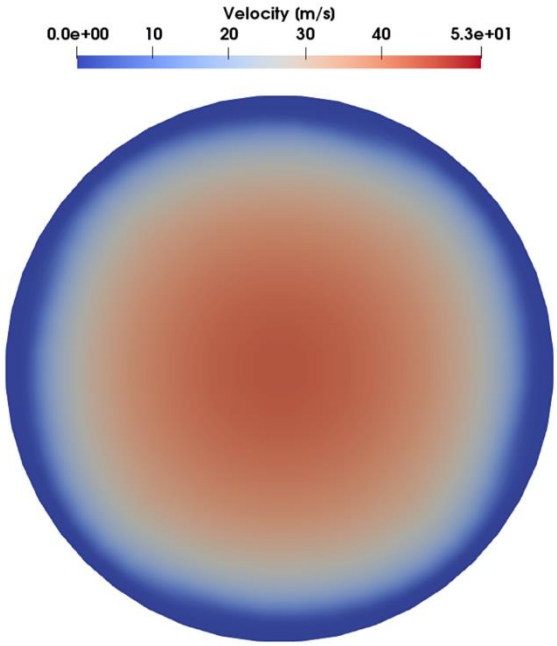


c) 0,44 [m]

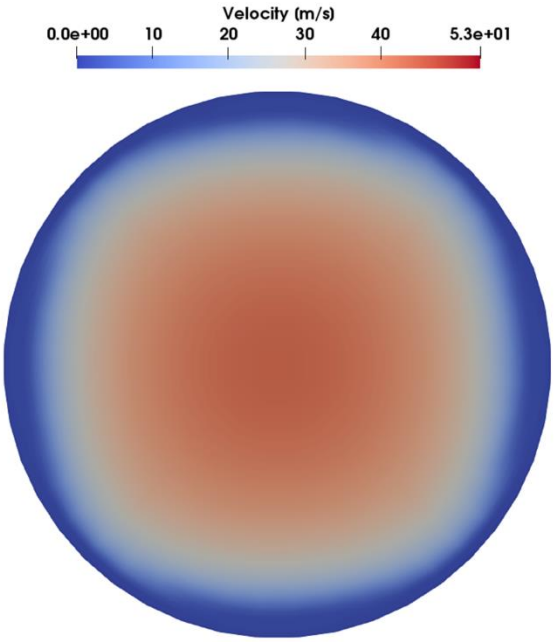


d) 0,94 [m]

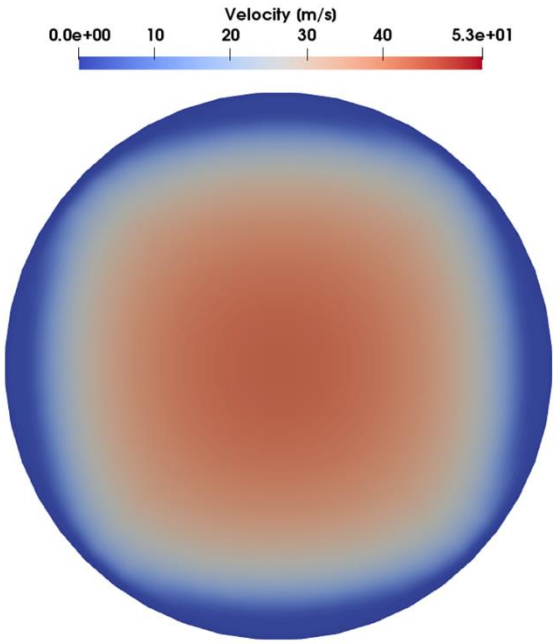


e) 1,07 [m]

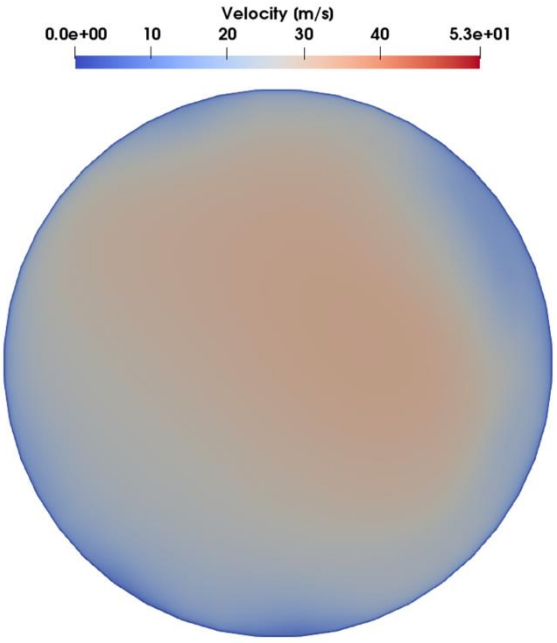


f) 3,85 [m]

Source: Author (2020).

## 5.2 Case 2

The second flow analyzed is similar to the first one, however, a droplet diameter equal to $10 \times 10^{-6}$ [m] was used for the dispersed phase. The behavior of the pressure distribution as a function of time was similar to the previous case, varying only the magnitudes of the pressure values and, therefore, were omitted here. The boundary conditions applied for this case were presented in the first column of Table 3.

Figure 16 shows a comparison between the experimental and numerical pressure in 7 planes along the pipe for the last two seconds (3 – 5 [s]) with differences up to 9,5%. Through this figure, it is possible to observe that the average pressure along the pipe presents less differences, when compared to the previous case. The dispersed phase diameter is directly related to the calculation of the drag force and, comparing the Figures 12 and 16, it is possible to observe that this parameter has significant influences on the flow. Unfortunately, it was not found any work related to annular flows that had an average value or an equation to estimate the diameter of the dispersed liquid phase.

Figure 16 - Numerical and experimental mean pressure for the Case 2.

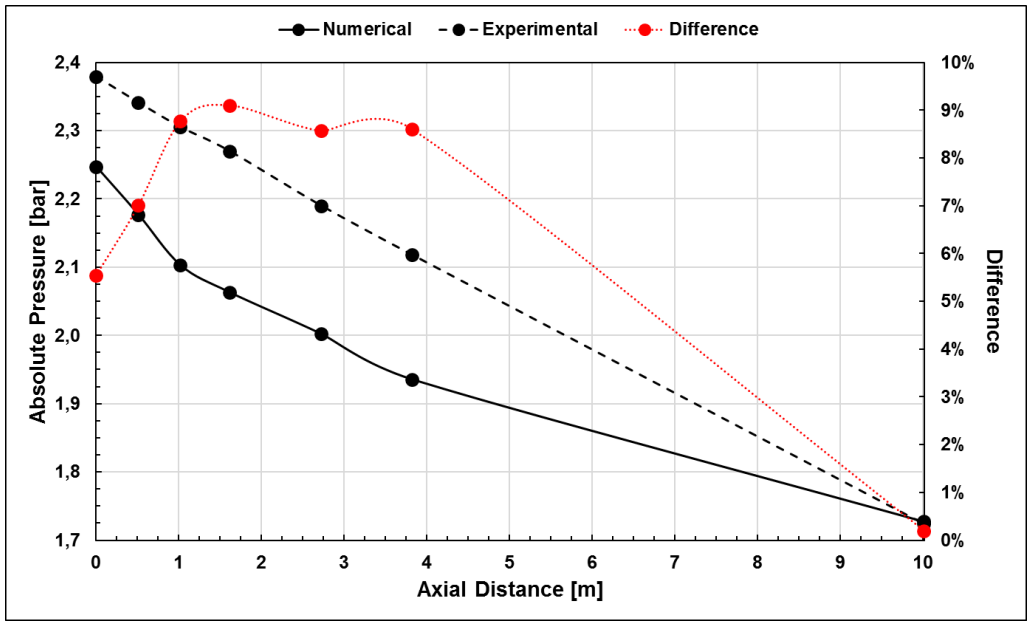


Source: Author (2020).

Figure 17 shows the variation of the mean void fraction as function of time for 6 planes along the pipe.

Figure 17 - Mean void fraction as function of time for the Case 2.

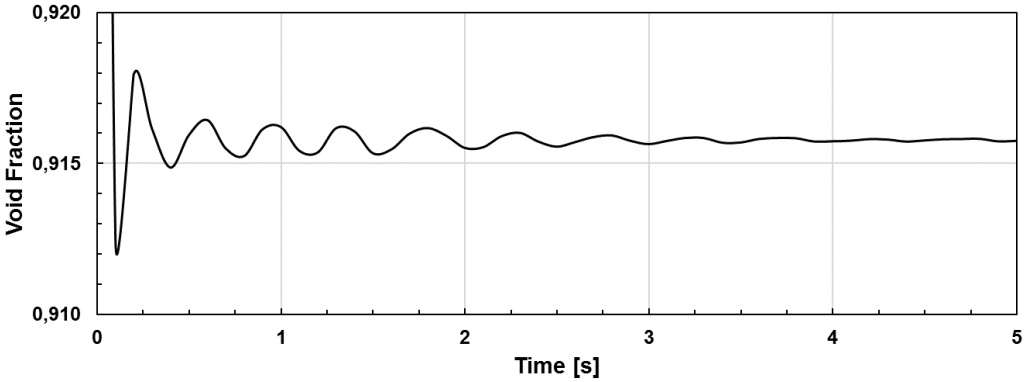


a) Plane positioned at 0,05 [m] from the inlet.

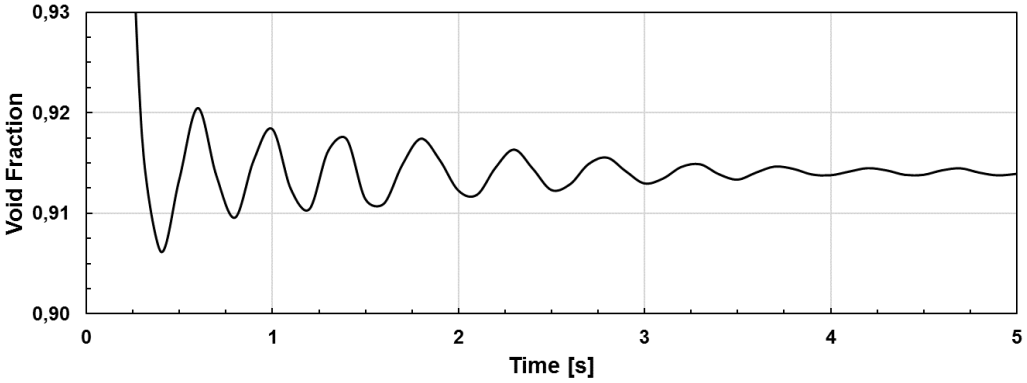


b) Plane positioned at 0,25 [m] from the inlet.

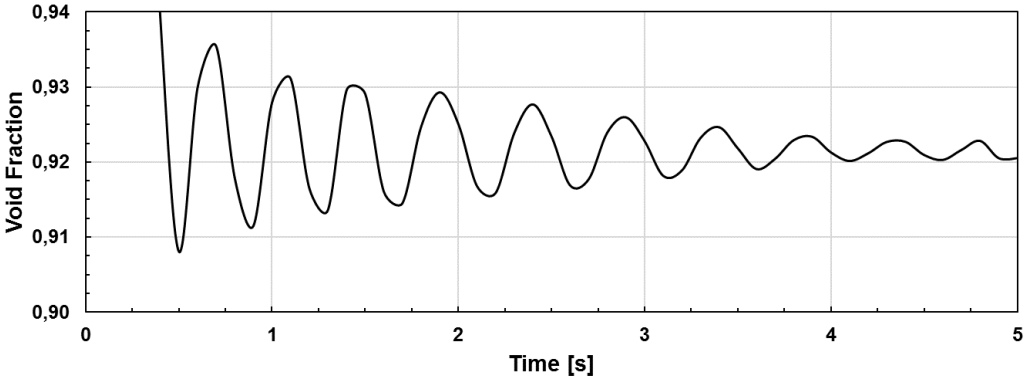


c) Plane positioned at 0,44 [m] from the inlet.

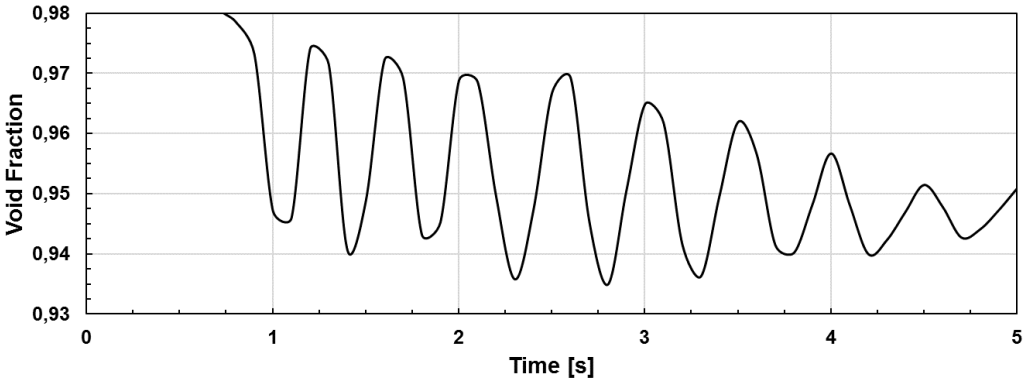


d) Plane positioned at 0,94 [m] from the inlet.

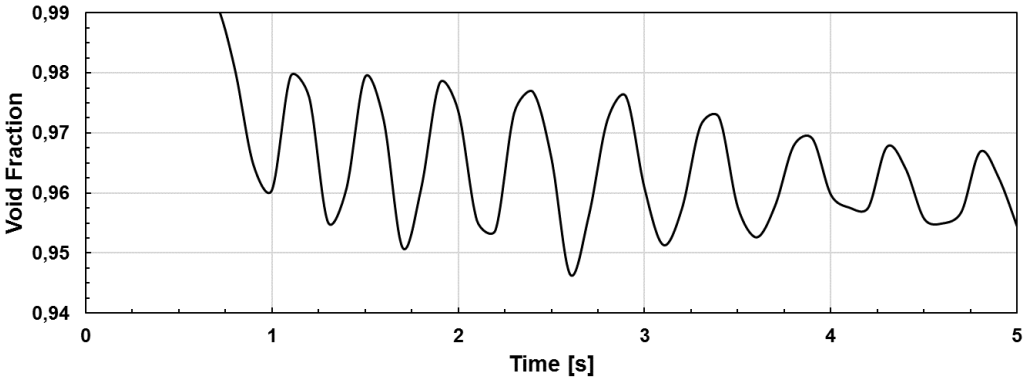


e) Plane positioned at 1,07 [m] from the inlet.

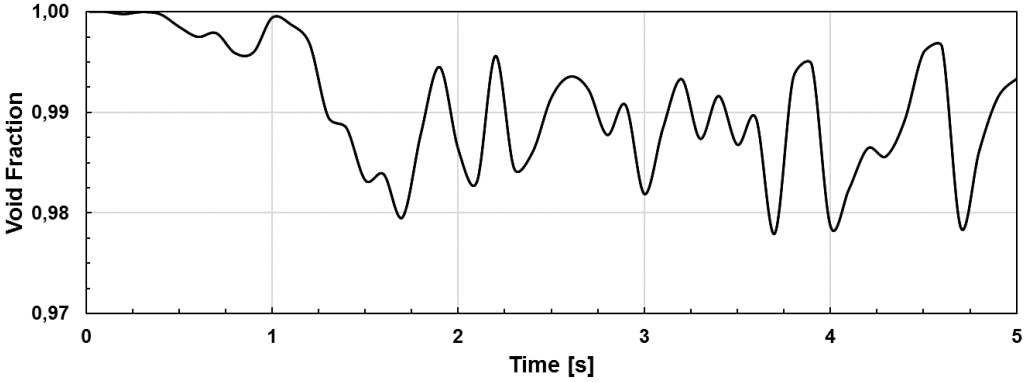


f) Plane positioned at 1,07 [m] from the inlet.

Source: Author (2020).

Comparing the Figures 13 and 17, the current case, in general, presents void fractions greater than the previous case, for corresponding plans. This means that with the decrease of the droplet's diameter, there is a decrease in the liquid film thickness. This behavior is

consistent with the physics, because the smaller the diameter of the dispersed phase, the lower the surface tension that holds the droplets in the liquid film and, therefore, it is easier to pull out the liquid droplets from the disturbance waves crests. In Figure 17.d), it is possible to observe that the void fraction did not converge to a constant value. This means that in this region part of the liquid film has already been pulverized. The simulation of the present case showed greater deficiencies in capturing the liquid film when compared to the previous one.

Figure 18 shows the front view of 1.5 [m] of the pipe, from the inlet, for a numerical time equal to 5 [s], where it is possible to compare the height of the liquid film captured by the simulations in these first two cases.

Figure 18 - Front view of 1.5 [m] of the pipe wall for the first two cases, for a numerical time equal to 5 [s].

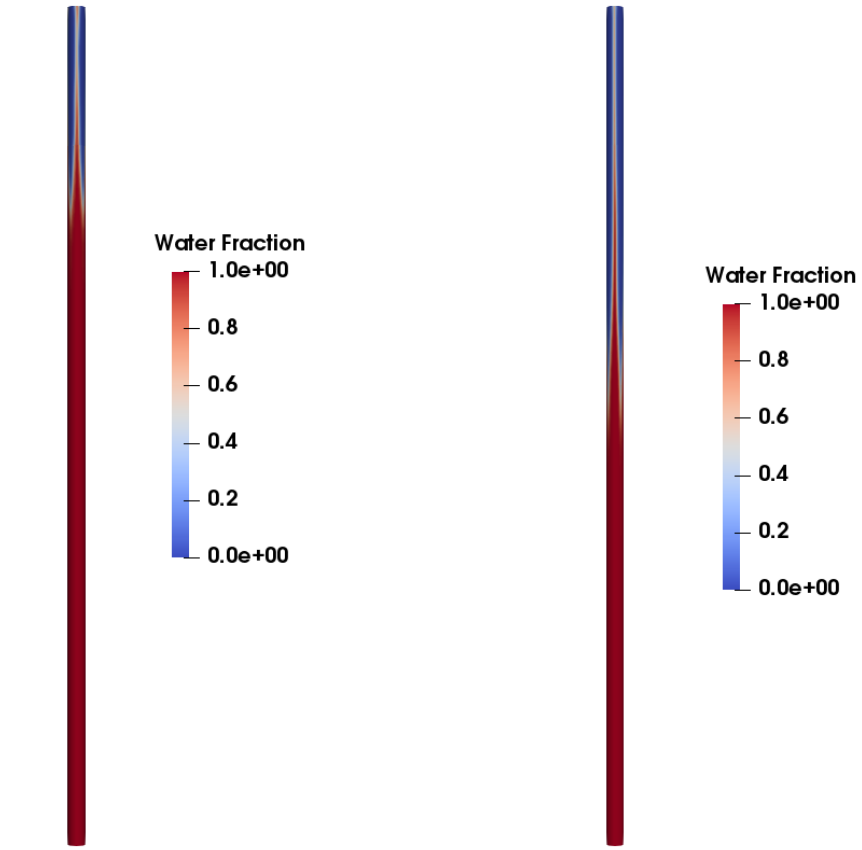


a) Case 1 b) Case 2

Source: Author (2020).

The figures referring to the distribution of the water fraction and the velocity profiles in the cross-sections are similar to the previous case and have been omitted here. The comparison between the numerical and experimental liquid film thickness was also omitted here, because, in the present simulation, there are few points for comparison, since the liquid film started to pulverize before 0.94 [m].

## 5.3 Case 3

The third flow analyzed has air and liquid mass fluxes equals to 71 and 60 [kg / m².s], respectively. A droplet diameter for the dispersed phase and a Courant number equals to $50 \times 10^{-6}$ [m] and 0.25, respectively, were used in this simulation. The behavior of the pressure distribution as a function of time was similar to Case 1, varying only the magnitudes of the pressure values and, therefore, were omitted here. The boundary conditions applied for this case were presented in the second column of Table 3.

Figure 19 - Numerical and experimental mean pressure for the Case 3.

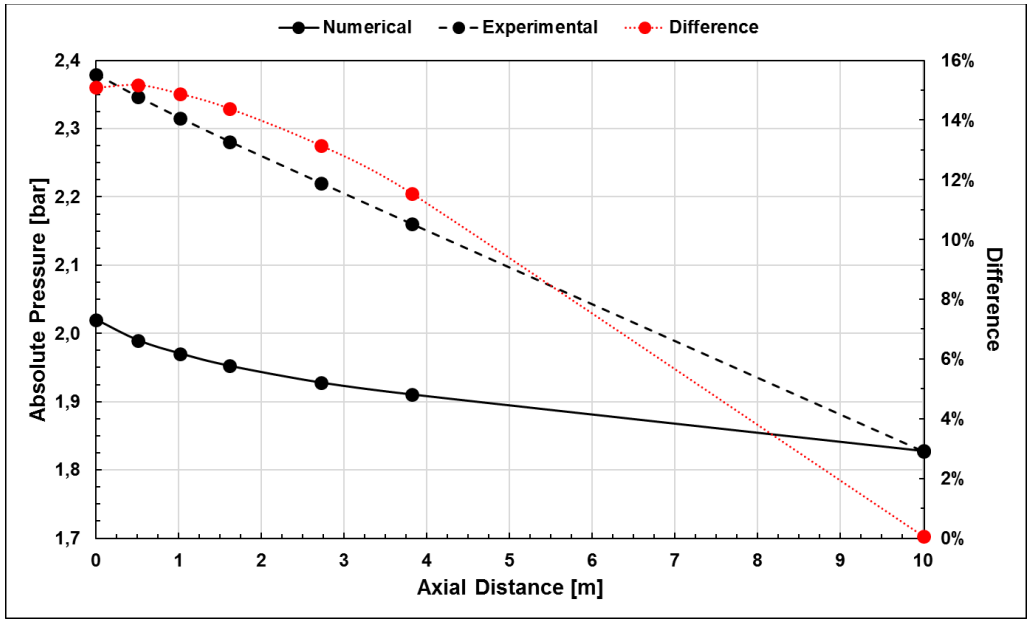


Source: Author (2020).

Figure 19 shows a comparison between experimental and numerical pressure in 7 planes along the pipe for the last two seconds (3 – 5 [s]) with differences up to 15%. Comparing Figures 12, 16 and 19, it is possible to observe that the current case presented the biggest differences. The liquid mass flux from this flow is half the one that was used in the two previous cases. Consequently, the accelerations within this flow are greater and, therefore, the disturbance waves appear earlier. However, as previously mentioned, the numerical simulations are having difficulties in correctly capturing the interface between the two phases from the moment that the disturbance waves appear and, thus, this is the reason why this case presented greater differences in relation to the previous ones.

Figure 20 shows the variation of the mean void fraction as function of time for 6 planes along the pipe

Figure 20 - Mean void fraction as function of time for the Case 3.

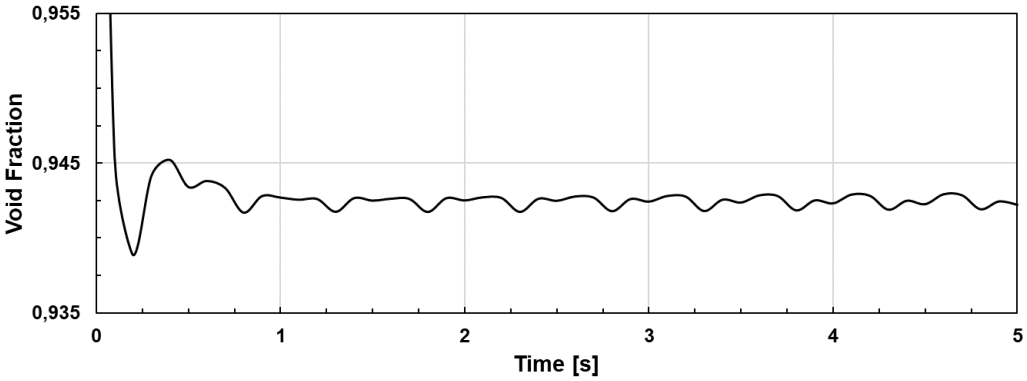


a) Plane positioned at 0,05 [m] from the inlet.

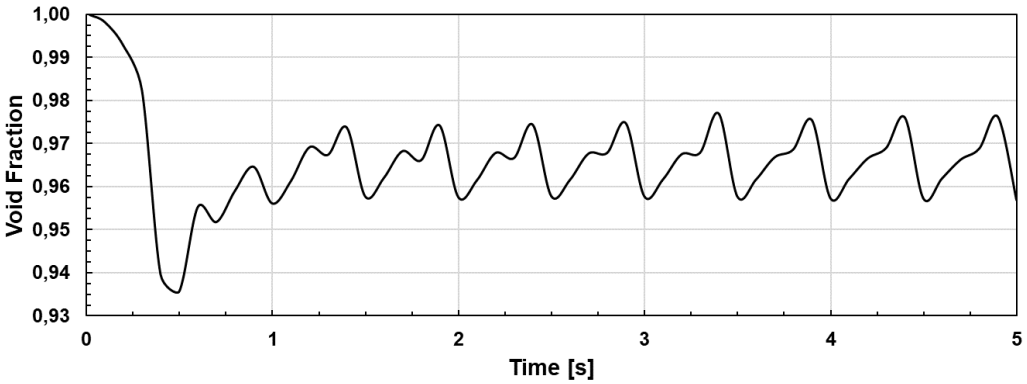


b) Plane positioned at 0,25 [m] from the inlet.

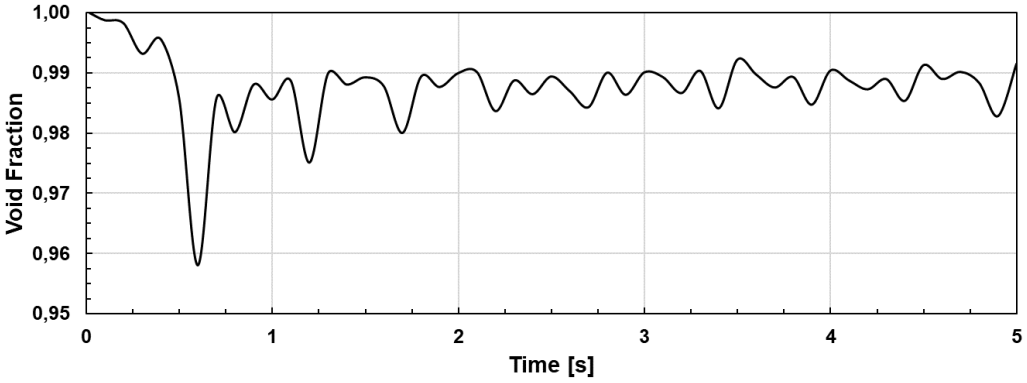


c) Plane positioned at 0,44 [m] from the inlet.

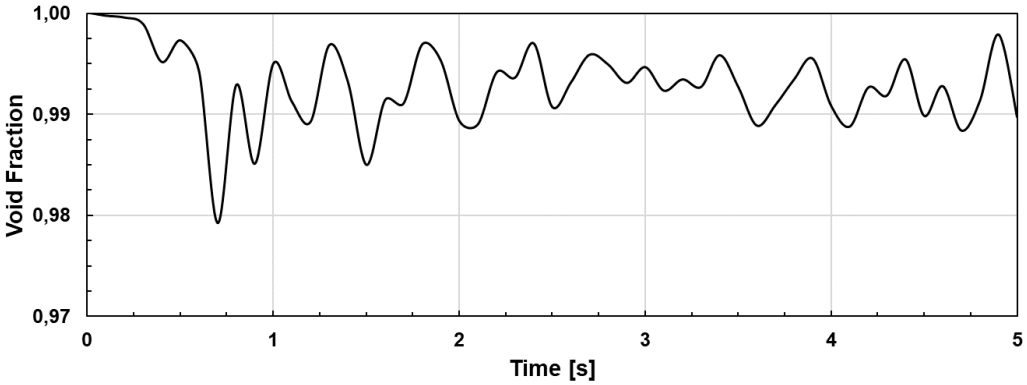


d) Plane positioned at 0,94 [m] from the inlet.

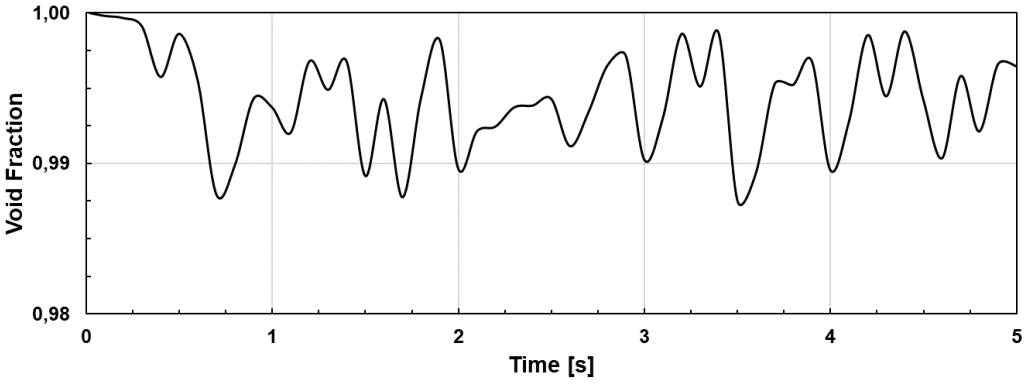


e) Plane positioned at 1,07 [m] from the inlet.

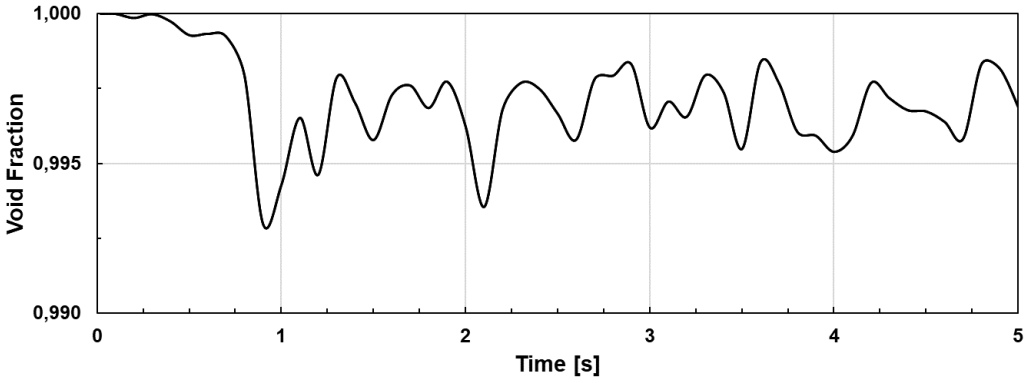


f) Plane positioned at 3,85 [m] from the inlet.

Source: Author (2020).

The void fraction of the present case, in general, is greater than that obtained in the first one, for corresponding plans. This behavior was already expected, since the air mass flux in both cases is the same, however, the liquid mass flux in the current flow is half that used in the first one.

In the second plane, Figure 20.b), it is possible to observe that the void fraction is not converging to a constant value and part of the liquid film has already been pulverized. This is a consequence of the precipitous appearance, in relation to the previous cases, of disturbance waves in the flow. In the subsequent planes, the void fraction already reaches levels close to 99%, that is, from the position of 0.44 [m] almost all the liquid film has already been pulverized.

The figures referring to the distribution of the water fraction and the velocity profiles in the cross-sections are similar to the Case 1 and have been omitted here. The comparison between the numerical and experimental liquid film thickness was also omitted here, because, in the present simulation, there are few points for comparison, since the liquid film started to pulverize before 0.25 [m].

## 5.4 Case 4

The fourth flow analyzed has air and liquid mass fluxes equals to 97 and 120 [kg / m².s], respectively. A droplet diameter for the dispersed phase and a Courant number equals to $50 \times 10^{-6}$ [m] and 1, respectively, were used in this simulation. In the present case, it was necessary to change the Courant number, since, by increasing the air mass flow rate, the air velocities increase and, consequently, the time step required for each iteration in the simulations decreases, which resulted in extremely high computational costs to perform this simulation with a Courant number equal to 0.25. So, to compensate this problem, it was decided to change the number of Courant in order to increase the time step and, thus, decrease the computational cost necessary to carry out this simulation.

The behavior of the pressure distribution as a function of time was similar to the Case 1, varying only the magnitudes of the pressure values and, therefore, were omitted here. The boundary conditions applied for this case were presented in the third column of Table 3. Figure 21 shows a comparison between the experimental and numerical pressure in 7 planes along the pipe for the last two seconds (3 – 5 [s]) with differences up to 12%.

Figure 21 - Numerical and experimental mean pressure for the Case 4.

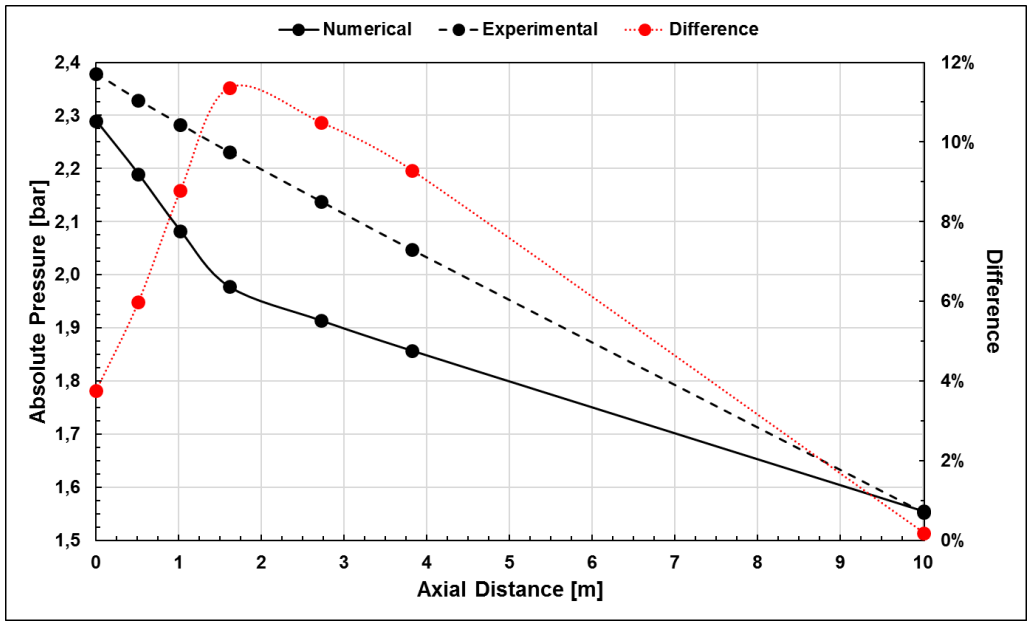


Source: Author (2020).

Figure 22 shows the variation of the mean void fraction as function of time for 6 planes along the pipe.

Figure 22 - Mean void fraction as function of time for the Case 4.

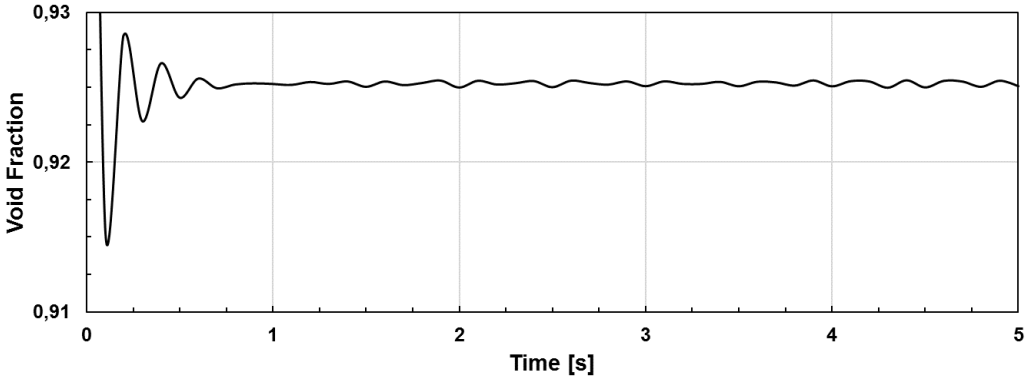


a) Plane positioned at 0,05 [m] from the inlet.

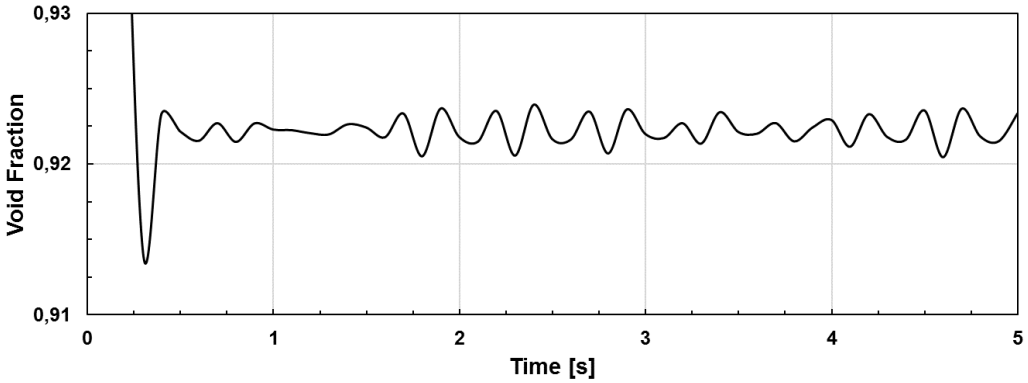


b) Plane positioned at 0,25 [m] from the inlet.

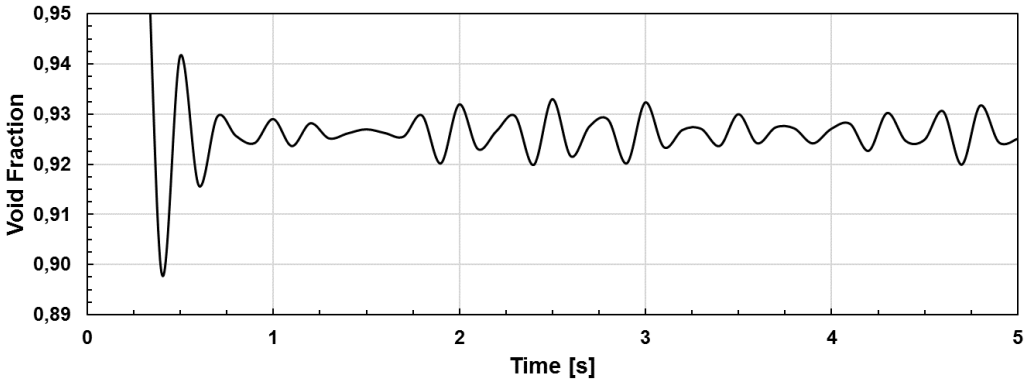


c) Plane positioned at 0,44 [m] from the inlet.

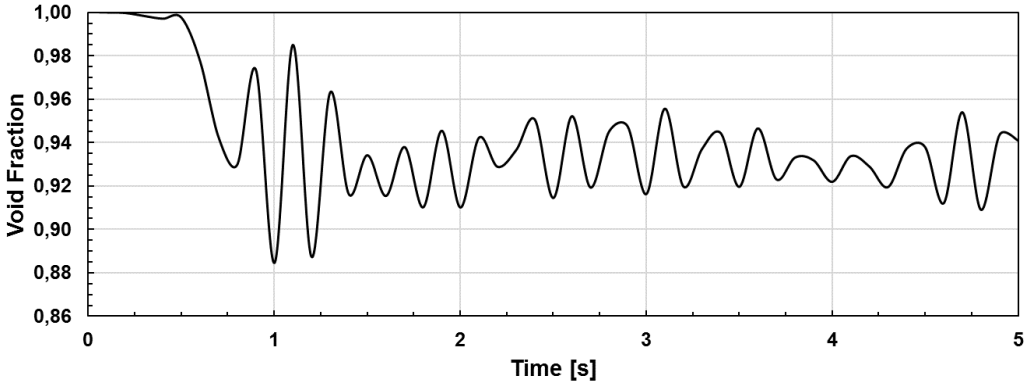


d) Plane positioned at 0,94 [m] from the inlet.

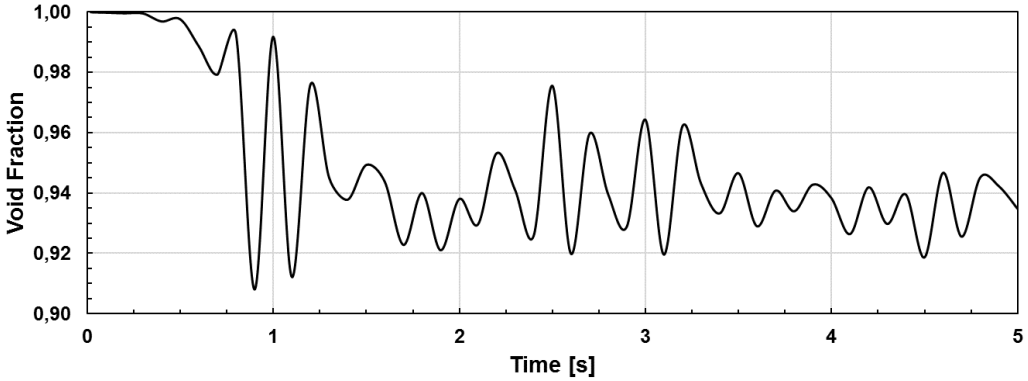


e) Plane positioned at 1,07 [m] from the inlet.

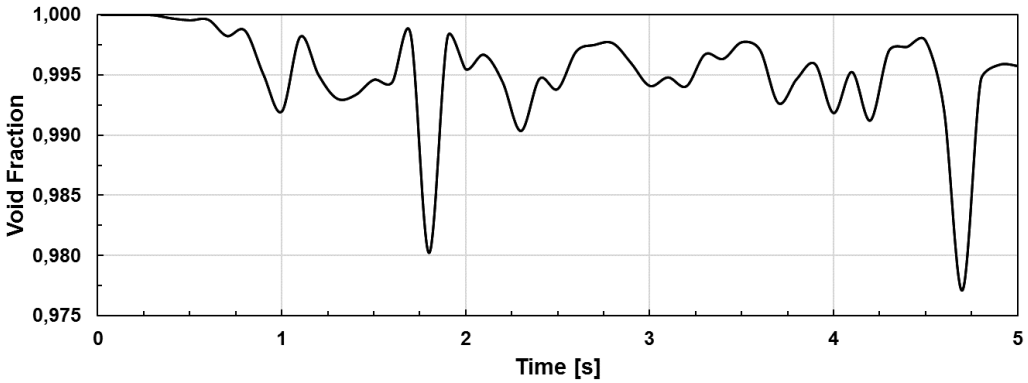


f) Plane positioned at 3,85 [m] from the inlet.

Source: Author (2020).

The void fraction of the present case, in general, is greater than that obtained in the first one, for corresponding plans. This behavior was also expected, since the water mass flux

in both cases is the same, however, the air mass flux in the current flow is greater than that used in the first one.

The figures referring to the distribution of the water fraction and the velocity profiles in the cross-sections are similar to the Case 1 and have been omitted here. Table 5 presents a comparison between the numerical and experimental liquid film thickness, where numerical results were obtained by averaging the last second (4 – 5[s]) of the simulation. The same procedure used to obtain the liquid film thickness of the numerical simulations in the Case 1 was applied here.

Table 5 - Comparison between the numerical and experimental liquid film thickness for the Case 4.

| **Position** | **Thickness** | |
|---|---|---|
| | **Experimental** | **Numerical** |
| **[m]** | **[mm]** | **[mm]** |
| 0,05 | 0,419 | 0,596 |
| 0,25 | 0,440 | 0,583 |
| 0,44 | 0,415 | 0,524 |
| 0,94 | 0,346 | 0,448 |

Source: Author (2020).

In this table, it is possible to observe that the numerical liquid film thicknesses, for this case, were also overestimated in relation to the experimental ones. The simulations in this case were not able to capture the increase of the liquid film thickness in the second plane that occurred in the experiments. In general, in the regions where the simulation was able to capture the liquid film, the numerical results were in agreement with the experimental ones.

# 6 CONCLUSIONS

This work aimed to study annular flows in vertical pipes numerically using the OpenFoam software. Initially, a bibliographic study was carried out regarding annular flows, where two works stood out for the elaboration of this thesis. The first one was the experimental study carried out by WOLF, JAYANTI and HEWITT (2001), which was used as a base case for the elaboration of the numerical simulations. The second work was the numerical study accomplished by TOCCI (2016), which was used as a guide for using the OpenFoam software. Then, the mathematical modeling implemented in the software that was used to solve the flows discussed here was presented. The boundary conditions and some flow properties necessary to perform the simulations were also presented throughout the text. Finally, 4 numerical simulations of annular flows were carried out, all based on the experimental study of WOLF, JAYANTI and HEWITT (2001).

The numerical simulations carried out in the present work presented some problems in capturing the interface between the two phases from a certain position along the pipe. Unfortunately, it was not possible to study all the suspicions that generated this problem due to the lack of computational resources. However, it is strongly believed that the quality of the mesh was the main factor that caused this deficiency in capturing the interface between the two phases from the moment that the disturbances waves start to appear in the flow.

As a final analysis of the simulations, it is possible to conclude that the method available in OpenFoam is capable of representing the physics involved in annular flow from a global point of view. Global parameters such as void fraction and pressure drop were calculated within ± 20% of the experimental values which can be considered reasonable for two-phase flows.

The use of high-end High-Performance Computing would be a necessity to this kind of simulation. The use of the SGI/Altix supercomputer at CENAPAD-SP was intended to solve this issue. However due to a malfunction during beginning of the year this equipment became offline, only returning to operation in late November. Several tests were performed using the platform, but due to the different architectures and the need for the installation of several

libraries for OpenFoam to work (that required assistance of the tech support) it was not possible to run any simulations yet.

As suggestions for future works, it would be interesting to elaborate an algorithm to perform the calculation of the interface Courant number within the multiphaseEulerFoam application to verify if it is possible to perform these simulations with bigger time steps. Other options would be to perform these simulations using parts of the test sections, try to simulate shorter pipes or to use other fluids that reach the annular flow pattern with lower velocities.

# REFERENCES

ABDULKADIR, M. **Experimental and computational fluid dynamics (CFD) studies of gas-liquid flow in bends.** 2011. 235 p. PhD Thesis - University of Nottingham, Nottingham, 2011.

ADAZE, E.; BADR, H.M.; AL-SARKHI, A. **CFD modeling of two-phase annular flow toward the onset of liquid film reversal in a vertical pipe.** Journal of Petroleum Science and Engineering**,** p. 755-774, 2019.

AL-SARKHI, A.; SARICA, C.; QURESHI, B. **Modeling of droplet entrainment in co-current annular two-phase flow: A new approach.** International Journal of Multiphase Flow, p. 21-28, 2012.

ALVES, M. V. C. **Modelagem numérica do escoamento transiente churn-anular em tubulações verticais e sua aplicação na simulação de carga de líquido em poços de gás.** 2014. 287 p. PhD Thesis – Federal University of Santa Catarina, Florianópolis, 2014.

ALVES, M. V. C. et al. **Modeling transient churn-annular flows in a long vertical tube.** International Journal of Multiphase Flow, p. 399-412, 2017.

ALIYU, A. M.; BABA, Y. D.; LAO, L.; YEUNG, H.; KIM, K. C. **Interfacial friction in upward annular gas–liquid two-phase flow in pipes.** Experimental Thermal and Fluid Science, p. 90-109, 2017.

ANSYS INC. (United States). **ANSYS Fluent User's Guide,** 2013. 2692 p.

BERTODANO, M. A. L.; JAN, C.; BEUS, S. G. **Annular flow entrainment rate experiment in a small vertical pipe.** Nuclear Engineering and Design, p. 61-70, 1997.

BARBOSA, J. R. **Phase change of single component fluids and mixtures in annular flowPhase change of single component fluids and mixtures in annular flow.** 2001. 435 p. PhD Thesis - Imperial College London, 2001.

BIRD, R. Byron; STEWART, Warren E.; LIGHTFOOT, Edwin N. **Transport Phenomena.** 2. ed.: John Wiley & Sons, Inc., 2002. 914 p.

BRACKBILL, J. U.; KOTHE, D. B.; ZEMACH, C. **A continuum method for modeling surface tension.** Journal of Computational Physics, p. 335-354, 1992.

CACHARD, F. D.; DELHAYE, J. M. **A slug-churn flow model for small-diameter airlift pumps**. International Journal Multiphase Flow. Great Britain, p. 627-649. feb. 1996.

ÇENGEL, Yunus A.; CIMBALA, John M. **Fluid mechanics: Fundamentals and applications.** 3. ed.: Mcgraw-hill, 2014. 1031 p. 1031 f.

CERNE, G.; PETELIN, S.; TISELJ, I. **Coupling of the interface tracking and the two-fluid models for the simulation of incompressible two-phase flow.** Journal of Computational Physics. p. 776-804, 2001.

CHEN, S. W.; LIN, M. S.; KUO, F. J.; CHAI, M. L.; LIU, S. Y.; LEE, J. D.; PEI, B. S. **Experimental investigation and identification of the transition boundary of churn and annular flows using multi-range differential pressure and conductivity signals.** Applied Thermal Engineering, p. 1275-1286, 2017.

COURANT, R.; FRIEDRICHS, K.; LEWY, H. **Über die partiellen Differenzengleichungen der mathematischen Physik.** In: MATHEMATISCHE ANNALEN, 1928. v. 100, p. 32 - 74.

CROWE, C. T. **Multiphase flow handbook.** Taylor & Francis Group, 2006. 1128 p.

GREENSHIELDS, Christopher J. **User Guide.** 6. ed.: OpenFoam Foundation Ltd, 2018. 237 p.

GUPTA, R.; TURANGAN, C. K.; MANICA, R. **Oil-water core-annular flow in vertical pipes: A CFD study.** The Canadian Journal of Chemical Engineering, p. 980-987, may 2016.

LANE, J. W.; AUMILLER, D. L. Jr; CHEUNG, F. B.; HOCHREITER, L. E. **A self-consistent three-field constitutive model set for predicting co-current annular flow.** Nuclear Engineering and Design, p. 3294-3308, 2010.

LIU, F. **A thorough description of how wall functions are implemented in OpenFoam.** In: PROCEEDINGS OF CFD WITH OPENSOURCE SOFTWARE, 2017.

LIU, L.; BAI, B. **Generalization of droplet entrainment rate correlation for annular flow considering disturbance wave properties.** Chemical Engineering Science, p. 279-291, 2017.

LIU, Y.; LI, W.Z.; QUAN, S.l. **A self-standing two-fluid CFD model for vertical upward two-phase annular flow.** Nuclear Engineering and Design, p. 1636-1642, 2011.

MATHIEU, J. M.; SCOTT, J. **An introduction to turbulent flow.** 1. ed. Cambridge: Cambridge University Press, 2000. 386 p.

MENTER, F. R.; KUNTZ, M.; LANGTRY, R. **Ten years of industrial experience with the sst turbulence model.** Turbulence, Heat and Mass Transfer, 2003.

PARSI, M.; AGRAWAL, M.; SRINIVASAN, V.; VIEIRA, R. E.; TORRES, C. F.; MCLAURY, B. S.; SHIRAZI, S. A.; SCHLEICHER, E.; HAMPEL, U. **Assessment of a hybrid CFD model for simulation of complex vertical upward gas–liquid churn flow.** Chemical Engineering Research and Design. p. 71-84, 2016.

PAGAN, E. V.; WALTRICH, P. J. **A simplified model to predict transient liquid loading in gas wells.** Journal of Natural Gas Science And Engineering, p. 372-381, 2016.

PAGAN, E.; WILLIAMS, W.C.; KAM, P.; WALTRICH, P.J. **A simplified model for churn and annular flow regimes in small- and large-diameter pipes.** Chemical Engineering Science, p. 309-321, 2017.

PEREZ, H. V.; ABDULKADIR, M.; AZZOPARDI, B.J. **grid generation issues in the CFD modelling of two-phase flow in a pipe.** Journal of Computational Multiphase Flows, p. 13-26. 2011.

POSADA, C.; WALTRICH, P. J. **Similarities and differences in churn and annular flow regimes in steadystate and oscillatory flows in a long vertical tube.** Experimental Thermal and Fluid Science, p. 272-284, 2018.

PRAUSNITZ, J. M.; LICHTENTHALER, R. N.; AZEVEDO, E. G. **Molecular thermodynamics of fluid-phase equilibria.** 3. ed. New Jersey: Prentice Hall, 1998. 864 p.

SCHILLER, L.; NAUMANN, A. **A drag coefficient correlation.** Zeitschrift Des Vereins Deutscher Ingenieure, p. 318-320, 1935.

TAITEL, Y.; BORNEA, D.; DUKLER, A. E. **Modelling flow pattern transitions for steady upward gas-liquid flow in vertical tubes.** Alche Journal, p. 345-354, may, 1980.

TEKAVČIČ, M.; KONČAR, B.; KLJENAK, I. **Three-dimensional simulations of liquid waves in isothermal vertical churn flow with OpenFoam.** Experimental and Computational Multiphase Flow, p. 300-306, 2019.

THAKER, J. P.; BANERJEE, J. **Cfd simulation of two-phase flow phenomena in horizontal pipelines using OpenFoam.**

TOCCI, F. **Assessment of a hybrid VOF two-fluid CFD solver for simulation of gas-liquid flows in vertical pipelines in OpenFoam.** 2016. 100 f. Masters Dissertation - Politecnico di Milano, Milan, 2016.

TURNER, R. G.; HUBBARD, M. G.; DUKLER, A.E. **analysis and prediction of minimum flow rate for the continuous removal of liquids from gas wells.** Journal of Petroleum Technology, p. 1475-1482. nov. 1969.

VAN NIMWEGEN, A.T.; PORTELA, L.M.; HENKES, R.A.W.M. **Modelling of upwards gas-liquid annular and churn flow with surfactants in vertical pipes.** International Journal of Multiphase Flow, p. 1-14, 2018.

WALLIS, G. **One-dimensional two-phase flow.** New York: Mcgraw-hill, 1969. 409 p.

WALTRICH, P. J.; FALCONE, G.; BARBOSA, J. R. **Axial development of annular, churn and slug flows in a long vertical tube.** International Journal of Multiphase Flow, p. 38-48, 2013.

WALTRICH, P. J.; FALCONE, G.; BARBOSA, J. R. **Liquid transport during gas flow transients applied to liquid loading in long vertical pipes.** Experimental Thermal and Fluid Science, p. 652-662, 2015.

WARDLE, K. E.; WELLER, H. G. **Hybrid multiphase CFD solver for coupled dispersed/segregated flows in liquid-liquid extraction.** International Journal of Chemical Engineering, 12 p., 2013.

WOLF, A.; JAYANTI, S.; HEWITT, G. F. **Flow development in vertical annular flow.** Chemical Engineering Science, v. 56, n. 10, p. 3221–3235, 2001.